AGU PUBLICATIONS

JGR

Journal of Geophysical Research: Atmospheres

RESEARCH ARTICLE
10.1002/2016JD024851

Key Points:
- Particle-resolved cloud parcel simulations resolving aerosol mixing state are performed
- Importance of black carbon particles mixing state is examined for various environmental conditions
- Errors in predicting cloud microphysical properties without resolving mixing state are reported

Correspondence to:
N. Riemer,
nriemer@illinois.edu

Citation:
Ching, J., N. Riemer, and M. West (2016), Black carbon mixing state impacts on cloud microphysical properties: Effects of aerosol plume and environmental conditions, *J. Geophys. Res. Atmos.*, *121*, 5990–6013, doi:10.1002/2016JD024851.

Received 23 JAN 2016
Accepted 30 APR 2016
Accepted article online 11 MAY 2016
Published online 31 MAY 2016

Black carbon mixing state impacts on cloud microphysical properties: Effects of aerosol plume and environmental conditions

J. Ching[1], N. Riemer[2], and M. West[3]

[1]Atmospheric Sciences and Global Change Division, Pacific Northwest National Laboratory, Richland, Washington, USA, [2]Department of Atmospheric Sciences, University of Illinois at Urbana–Champaign, Urbana, Illinois, USA, [3]Department of Mechanical Science and Engineering, University of Illinois at Urbana–Champaign, Urbana, Illinois, USA

Abstract Black carbon (BC) is usually mixed with other aerosol species within individual aerosol particles. This mixture, along with the particles' size and morphology, determines the particles' optical and cloud condensation nuclei properties, and hence black carbon's climate impacts. In this study, the particle-resolved aerosol model PartMC-MOSAIC (Particle Monte Carlo-Model for Simulating Aerosol Interactions and Chemistry) was used to quantify the importance of black carbon mixing state for predicting cloud microphysical quantities. Based on a set of about 100 cloud parcel simulations a process-level analysis framework was developed to attribute the response in cloud microphysical properties to changes in the underlying aerosol population ("plume effect") and the cloud parcel cooling rate ("parcel effect"). In most of the simulations the plume and parcel effects had opposite signs, with the plume effect dominating. The response of cloud droplet number concentration to changes in BC emissions depended on the BC mixing state. When the aerosol population contained mainly aged BC, an increase in BC emission increased cloud droplet number concentrations ("additive effect"). In contrast, when the aerosol population contained mainly fresh BC particles, they act as sinks for condensable gaseous species, resulting in decreasing cloud droplet number concentration as BC emissions were increased ("competition effect"). Additionally, we quantified the error in cloud microphysical quantities when neglecting the information on BC mixing state. The errors ranged from −12% to +45% for the cloud droplet number fraction, from 0% to +1022% for the nucleation-scavenged BC mass fraction, from −12% to +4% for the effective radius, and from −30% to +60% for the relative dispersion.

1. Introduction

Black carbon-containing aerosol particles impact climate by a variety of pathways. They absorb solar radiation, which causes a warming of the atmosphere where these particles reside [*Jacobson*, 2001; *Seinfeld*, 2008; *Ramanathan and Carmichael*, 2008; *Feichter and Stier*, 2012]. They also can impact climate indirectly, owing to their interactions with clouds. For this paper two of these indirect effects are of particular importance [*Bond et al.*, 2013, Chapter 7], here named the "additive" and "competition" effects. First, even though fresh black carbon-containing particles (called "BC particles" in this paper for brevity) are poor cloud condensation nuclei, they can form cloud droplets if they are mixed with soluble aerosol material [*Hitzenberger et al.*, 1999; *Dusek et al.*, 2006; *Andreae and Rosenfeld*, 2008]. Increasing BC emissions would therefore result in an increase of cloud condensation nuclei (CCN) concentration (the additive effect). Second, precisely because BC particles act as a sink for condensable soluble material, increasing their number concentration may result in a decrease of CCN if the available condensable material is limited (the competition effect). The competition between these climate impacts of BC particles makes it difficult to estimate the overall impact of black carbon mitigation strategies [*Chen et al.*, 2010; *Jacobson*, 2010; *Bahadur et al.*, 2012; *Wang et al.*, 2014].

Whether a BC particle forms a cloud droplet hinges on its critical supersaturation and the ambient saturation ratio. The former depends on the size and hygroscopicity of the BC particle, which are in turn determined by the state of the particle at emission and the aging processes that the particle is exposed to in the atmosphere [*Furutani et al.*, 2008; *Riemer et al.*, 2010]. The latter is determined by the characteristics of the entire aerosol population as well as the environmental updraft speed [*Feingold et al.*, 2003; *Reutter et al.*, 2009; *Lu et al.*, 2012]. Field observations show that the distribution of chemical species across an aerosol population,

i.e., the aerosol mixing state, can be complex [*Moteki et al.*, 2007; *Moffet and Prather*, 2009; *McMeeking et al.*, 2011; *Cahill et al.*, 2012], which represents a considerable modeling challenge. Recent modeling efforts on the global scale [*Bauer et al.*, 2008; *Ma et al.*, 2012; *Liu et al.*, 2012] and regional scale [*Matsui et al.*, 2013; *Zhang et al.*, 2014] have refined the model representation of aerosol mixing state; however, simplifying assumptions regarding mixing state are still used in these models. We are only now beginning to systematically quantify the errors introduced by these assumptions [*Ching et al.*, 2012; *Kaiser et al.*, 2014].

In *Ching et al.* [2012], we used the stochastic particle-resolved model PartMC-MOSAIC [*Riemer et al.*, 2009; *Zaveri et al.*, 2008] for cloud parcel simulations and developed a method to quantify the errors in the activation of BC particles introduced by simplified aerosol mixing state representations. For a polluted urban plume scenario of 48 h of simulation time, neglecting differences in particle composition resulted in errors of less than 25% for the predictions of cloud droplet number fraction, while errors for the predictions in the nucleation-scavenged BC mass fraction were up to 600%. Generally, relatively small errors in cloud droplet number fraction did not necessarily translate to small errors in nucleation-scavenged BC mass fraction. However, these findings were based on only one particular urban plume scenario.

In this study, we use a more comprehensive approach to generalize the conclusions in *Ching et al.* [2012], investigating a wider range of environmental conditions. In addition, we devise a framework to quantify how mixing state affects the response in cloud droplet number concentration to changes in environmental conditions.

Specifically, we probe the parameter space by varying four parameters, namely, the BC emission rate, the background particle number concentration, the gas emission rate, and the cloud parcel cooling rate. The first three parameters influence the evolution of aerosol mixing state, i.e., how the aerosol particles age in the urban plume through coagulation and condensation of secondary aerosol species. This consequently affects the hygroscopicity and critical supersaturation distribution of the particle population. Together with the fourth parameter (cooling rate) this determines the maximum saturation ratio attained in the cloud parcel, which critically affects the cloud droplet number concentrations [*Feingold et al.*, 2003; *Reutter et al.*, 2009].

The contributions of this study are (1) developing a metric to attribute the differences in cloud droplet number concentration between any two environmental scenarios to differences in two separate factors, namely, the underlying aerosol population characteristics and the maximum saturation ratio attained in the cloud parcel; and (2) quantifying the sensitivity of the errors in calculating cloud microphysical properties due to simplified aerosol mixing state representation to a wide range of environmental conditions.

The paper is structured as follows. Section 2 introduces the particle-resolved model PartMC-MOSAIC and particle-resolved cloud parcel model. Section 3 describes the simulation setup. The results are then discussed in three separate sections. Section 4 presents an overview of the aerosol population characteristics of the suite of urban plume scenarios and summarizes the results from the cloud parcel simulations. In section 5, we present a method for attributing changes in cloud droplet number concentrations to changes in the initial aerosol population and to the cloud parcel response. Section 6 gives the error quantification in activation fraction, the associated nucleation-scavenged fraction of black carbon, the effective radius, and the relative spectral dispersion of cloud droplet spectrum due to simplified model representation in aerosol mixing states. Summary and conclusions are provided in section 7.

2. Model Description

2.1. Particle-Resolved Aerosol Model PartMC-MOSAIC

PartMC-MOSAIC (Particle Monte Carlo-Model for Simulating Aerosol Interactions and Chemistry) [*Riemer et al.*, 2009; *Zaveri et al.*, 2008] is a stochastic, particle-resolved model that simulates the evolution of the per-particle composition of a large number of aerosol particles within a well-mixed computational volume. The particle positions in the computational volume are not tracked. The full model description of PartMC-MOSAIC is given in *Riemer et al.* [2009]. In brief, PartMC-MOSAIC simulates the evolution of individual particle composition in an aerosol population due to both particle coagulation and gas-particle partitioning. While we track the number of coagulation events that each particle undergoes, we do not store the internal structure of the particles.

PartMC handles particle emission, mixing of particles with background air, as well as Brownian coagulation among particles stochastically [*Riemer et al.*, 2009]. Dry and wet deposition of aerosol particles are not included. We used weighted particles in the sense of *DeVille et al.* [2011] to increase computational efficiency.

To allow for the treatment of aerosol chemistry, PartMC is coupled to the aerosol chemistry module MOSAIC [*Zaveri et al.*, 2008]. This includes the gas phase photochemical mechanism CBM-Z [*Zaveri and Peters*, 1999], a method for estimating activity coefficients of electrolytes and ions in aqueous solutions [*Zaveri et al.*, 2005a], a solver for intraparticle solid-liquid partitioning [*Zaveri et al.*, 2005b], and a solver for dynamic gas-particle partitioning [*Zaveri et al.*, 2008]. MOSAIC includes 77 gaseous species and 19 aerosol species. The first 11 aerosol species are SO_4, NO_3, Cl, CO_3, MSA (methanesulfonic acid), NH_4, Na, Ca, other inorganic mass (which includes species such as SiO_2, metal oxides, and other unmeasured or unknown inorganic species present in aerosols), black carbon (BC), and primary organic aerosol (POA). To represent secondary organic aerosol (SOA) we use the SORGAM model [*Schell et al.*, 2001] with four model species originating from the oxidation of anthropogenic VOC precursors, and four model species from the oxidation of biogenic VOC precursors. The model version of PartMC that we used here is version 2.2.0.

2.2. Particle-Resolved Cloud Parcel Model

The details of the particle-resolved cloud parcel capability were described in *Ching et al.* [2012]. The cloud parcel model simulates the competition for water vapor among aerosol particles that experience cooling at a prescribed cooling rate. For an input aerosol population containing N_p particles, the system of ordinary differential equations consists of $N_p + 1$ equations, with one equation for the rate of change of the environmental saturation ratio, S_v and N_p equations for the rate of change of the wet diameter of each particle. For numerical details of the cloud parcel model implementation, the readers are referred to Appendix A in *Ching et al.* [2012]. We do not consider any entrainment and collision-coalescence among cloud droplets, and both temperature and pressure are prescribed functions of time.

In *Ching et al.* [2012] we prescribed the cooling rate, but assumed constant pressure. Here we updated the model to allow for pressure changes consistent with adiabatic conditions. To simplify the numerical implementation we precalculated the pressure along the trajectory as follows. During the subsaturated stage, the relationship between temperature and pressure is dry adiabatic. Once saturation is reached, we use pseudo-moist adiabatic conditions to describe the relationship between the temperature and pressure in the cloud parcel. The rate of change of parcel pressure, $\mathrm{d}p/\mathrm{d}t$, can be calculated from the constant cooling rate, $\mathrm{d}T/\mathrm{d}t$ as follows [*Pruppacher and Klett*, 1997],

$$\frac{\mathrm{d}p}{\mathrm{d}t} = \frac{(c_{pa} + w_v c_{pv})p}{(R_a + w_v R_v)T}\frac{\mathrm{d}T}{\mathrm{d}t} + \frac{l_v p}{(R_a + w_v R_v)T}\frac{\mathrm{d}w_v}{\mathrm{d}t}, \tag{1}$$

where w_v is water vapor mixing ratio, c_{pa} is the specific heat capacity of dry air, c_{pv} is the specific heat capacity of water vapor, R_a is the specific gas constant for dry air, and R_v is the specific gas constant for water vapor. We calculate $\mathrm{d}w_v/\mathrm{d}t$ using the Clausius-Clapeyron equation and the rate of change of temperature, $\mathrm{d}T/\mathrm{d}t$, assuming all water vapor condenses in the saturated environment. From $\mathrm{d}p/\mathrm{d}t$, together with the initial parcel pressure, a parcel pressure time series can be precalculated and used as cloud parcel model input.

The modeling approach used here follows *Majeed and Wexler* [2001] in prescribing the cooling rate. An alternative modeling framework would prescribe the updraft velocity and compute the temperature change, which it is done in many other cloud parcel studies [*Howell*, 1949; *Mordy*, 1959; *Pruppacher and Klett*, 1997; *Seinfeld and Pandis*, 1997; *Nenes et al.*, 2001; *Chen et al.*, 2016]. However, computing temperature changes would require the modeling of radiative heating effects due to the presence of black carbon inside the cloud droplets and as interstitial aerosol [*Conant et al.*, 2002], which would significantly complicate the interpretation of our results.

3. Description of Simulations

3.1. Plume Time Versus Parcel Time

Following the same strategy as in *Ching et al.* [2012], the simulations in this study were carried out as a two-stage process, the urban plume stage and the cloud parcel stage. For the urban plume stage, the evolution of an urban plume aerosol population in a subsaturated environment was simulated using PartMC-MOSAIC. This was done in a Lagrangian approach, assuming that the parcel moved over a polluted urban environment for 48 h, starting at 6:00 A.M. local time. We refer to the time-elapsed variable during the urban plume stage as *plume time* t_p, where $t_p = 0$ corresponds to the 6:00 A.M. starting time. An overview of the urban plume scenarios is provided in section 4.1. We focus our discussion on the particle populations at $t_p = 1$ h, 12 h, 24 h, and 48 h, as these represent very different stages regarding the degree of aging of

Table 1. Number Concentration, N_a, of the Initial/Background Aerosol Population and Area Source Strength, E_a, of the Three Types of Emission[a]

		D_g (μm)	σ_g	Composition by Mass
Initial/Background	N_a (cm^{-3})			
Aitken mode	1800	0.02	1.45	49.64% $(NH_4)_2SO_4$ + 49.64% SOA + 0.72% BC
Accumulation mode	1500	0.116	1.65	49.64% $(NH_4)_2SO_4$ + 49.64% SOA + 0.72% BC
Emission	E_a /m^{-2} s^{-1}			
Meat cooking	9×10^6	0.086	1.91	100% POA
Diesel vehicles	1.6×10^8	0.05	1.74	30% POA + 70% BC
Gasoline vehicles	5×10^7	0.05	1.74	80% POA + 20% BC

[a] All aerosol size distributions are assumed to be lognormal and defined by the geometric mean diameter, D_g, and the geometric standard deviation, σ_g.

BC-containing particles. Aging processes include coagulation among particles and condensation of secondary aerosol mass on existing aerosol particles, which result in changes in per-particle chemical composition. Photochemical aging is not considered in this study. The PartMC-MOSAIC model does not currently include photochemical aging, but it is the subject of current model development and will be investigated in a future study.

We then used the particle-resolved populations of the selected plume hours to initialize individual cloud parcel simulations that have a duration of 10 min each. We call the time variable during the cloud parcel stage *cloud parcel time* t_c, so that for any given cloud parcel simulation t_c runs from 0 min to 10 min. Since processes other than water vapor condensation and liquid water droplet evaporation were not included in the cloud parcel model simulation, any differences in cloud droplet number concentration and other associated cloud microphysical properties can be exclusively attributed to differences in the aerosol particle population characteristics that was used as input.

3.2. Setup of Sensitivity Simulations and Nomenclature

We constructed a scenario library of eight different scenarios as follows. Six 48 h urban plume scenarios were constructed by varying the emission rate of BC-containing particles (100%, 25%, and 2.5% of the case presented by *Ching et al.* [2012], denoted by E100, E25, and E2.5, respectively), and in the number concentration of background particles (100% and 10% of the case in *Ching et al.* [2012], denoted by B100 and B10, respectively). These variations changed the BC mixing state by changing the coagulation rates and competition for condensation of secondary aerosol species. The gas phase emissions for these six scenarios were the same as presented in *Ching et al.* [2012] (denoted by G100). The resulting BC mass concentrations were consistent with observations described in the Report to Congress on Black Carbon [*United States Environmental Protection Agency*, 2012, pp. 120–121], which states that BC concentrations in the U.S. range between 0.3 and 3.0 μg m^{-3} in urban areas and between 0.1 and 0.6 μg m^{-3} in rural areas.

Two more 48 h urban plume scenarios were added that varied in the emission rate of the gaseous components (50% and 25% of the original case in *Ching et al.* [2012], denoted by G50 and G25, respectively). The emission and background parameters for these two scenarios were kept at the base case (B100-E100). For all urban plume scenarios, both aerosol and gas phase emissions were introduced during the first 12 h of simulation. This setup is the same in *Zaveri et al.* [2010], and was chosen with the following conceptual model in mind. When the simulation starts at 6:00 A.M. LST (local solar time), the Lagrangian air parcel initially represents a volume of air in the polluted, well-mixed boundary layer during the daytime. After sunset we assume the air parcel represents the polluted air that remains in the nocturnal residual layer, decoupled from the stable surface layer, and hence we discontinue emissions after 12 h. By the next morning (around 0600 LST), the polluted air parcel is assumed to be over ocean, again decoupled from the stable marine surface layer, and is advected in the residual layer for another day.

As we will show in section 4.1, changing these input parameters created a wide range of urban plume conditions where BC aging proceeded at different rates. As shown in previous studies [*Riemer et al.*, 2010; *Fierce et al.*, 2015], the aging rate, i.e., the conversion of BC from hydrophopic to hygroscopic, is determined by both condensation of secondary aerosol and coagulation with more hygroscopic particles.

Table 2. Parameters That Were Varied to Construct a Total of 96 Cloud Parcel Simulations and the Corresponding Abbreviation Used in the Text[a]

	Quantity	Values (Abbreviations)			
Plume scenarios	Background particle concentration	100% (B100)	10% (B10)		
	BC particle emission rate	100% (E100)	25% (E25)	2.5% (E2.5)	
	Gas emission concentration	100% (G100)	50% (G50[b])	25% (G25[b])	
Cloud parcel simulations	Plume hour	1 h (T1)	12 h (T12)	24 h (T24)	48 h (T28)
	Cooling rate (in K min^{-1})	0.15 (C0.15)	0.5 (C0.5)	0.85 (C0.85)	

[a]For example, the abbreviation B10-E25-G100-T12-C0.15 refers to the cloud parcel simulation that was initialized with urban plume run with 10% background aerosol concentration, 25% BC emission rate and 100% gas emission rate at $t_p = 12$ h using a cooling rate of $\dot{T} = -0.15$ K min^{-1}.
[b]The scenarios that were only run in conjuction with scenario B100-E100.

The relative importance of these two processes depends on the particular environmental conditions. For our base case scenario (B100-E100), condensation dominated during the daytime, while coagulation dominated during the nighttime.

All other input parameters were identical for the urban plume scenarios. These included the initial chemical composition and the size distribution parameters of background particles and the particle emissions, as well as meteorological conditions such as temperature profile, relative humidity, and mixing height. The base case plume scenario (B100-E100-G100) was described in detail in *Ching et al.* [2012], and Table 1 summarizes the information regarding the background aerosol distributions and the particle emissions. The composition of freshly emitted BC particles from traffic is prescribed as 70% BC and 20% POA (representing emissions from diesel cars), and 20% BC and 80% POA (representing emissions from gasoline cars). Both BC and POA are assumed to be hydrophobic species with a hygroscopicity parameter of 0 for BC and of 0.001 for POA.

As outlined in section 3.1, we used four selected aerosol populations from each urban plume scenario as inputs for the cloud parcel simulations; these were the populations at $t_p = 1$ h, 12 h, 24 h, and 48 h, abbreviated by T1, T12, T24, and T48, respectively. Since the error magnitudes may also depend on the cooling rate that the aerosol populations are exposed to in the cloud parcel, we explored different cooling rates, 0.15 K min^{-1}, 0.5 K min^{-1}, and 0.85 K min^{-1}, denoted by C0.15, C0.5, and C0.85, respectively. The three cooling rates correspond approximately to cloud base updraft speeds of 0.55 m s^{-1}, 1.82 m s^{-1}, and 3.10 m s^{-1}, respectively, and were selected to represent conditions ranging from stratus [*Babb and Verlinde*, 1999; *Peng et al.*, 2005] to cumulus cloud types [*Lu et al.*, 2012]. The initial relative humidity of each cloud parcel simulation was 95%.

This amounts to 96 individual cloud parcel simulations in total (8 urban plume scenarios with 12 cloud parcel simulations each). Table 2 provides an overview and lists the abbreviations used for the remainder of this paper to refer to individual cases. For example, the abbreviation B10-E25-G100-T12-C0.15 refers to the cloud parcel simulation that was initialized with the urban plume scenario with 10% background aerosol number concentration, 25% BC emission rate, and 100% gas emission rate at plume time $t_p = 12$ h using a cooling rate of $\dot{T} = -0.15$ K min^{-1}.

4. Overview of Urban Plume Scenarios and Cloud Parcel Simulations

This section describes the range of aerosol concentration levels and aerosol population characteristics covered by the urban plume scenarios and presents a summary of the results of the associated cloud parcel simulations.

4.1. Urban Plume Scenarios

Figure 1 shows the time series of selected quantities from the urban plume scenarios. The line color indicates the level of the BC emissions (magenta for E100, light blue for E25, and yellow for E2.5), and the line style indicates the level of background particle concentration (solid for B100 and dashed for B10). For example, the yellow dashed line represents plume scenario B10-E2.5-G100.

The temporal variation of aerosol number concentration N_a in Figure 1a was governed by particle emission, coagulation and dilution. For all simulations the maximum number concentration was therefore reached

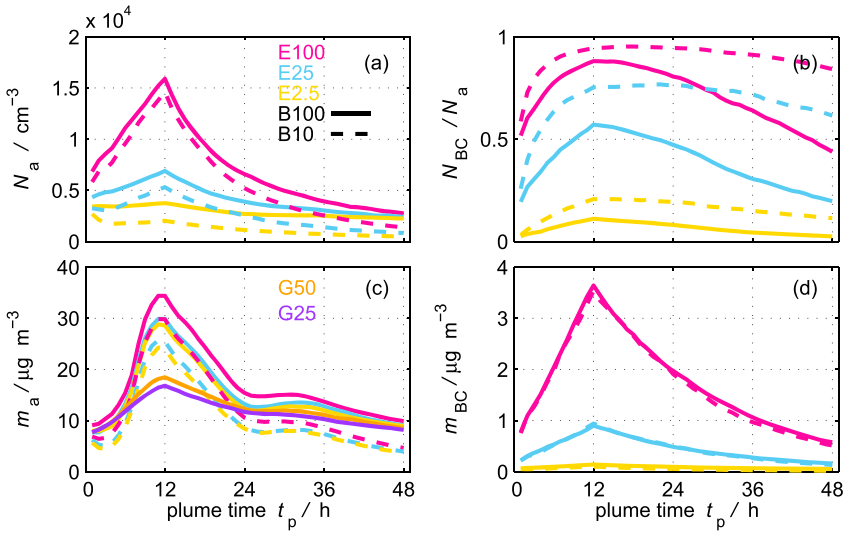

Figure 1. (a) Total aerosol number concentration, N_a, (b) ratio of BC-containing aerosol number concentration, N_{BC} to total aerosol number concentration, N_a, (c) total aerosol mass concentration, m_a (d) total BC-containing aerosol mass concentration, m_{BC}, as a function of plume time t_p. Magenta, blue, and yellow represent black carbon emission rate levels, E100, E25, and E2.5, respectively. Solid and dashed lines stand for background aerosol number concentrations, B100 and B10, respectively. In Figure 1c, the orange and purple solid lines indicate the total aerosol mass concentration, m_a, for B100-E100-G50 and B100-E100-G25.

at the end of the emission period, at $t_p = 12$ h. It ranged from 1.2×10^3 cm^{-3} for the least polluted case B10-E2.5-G100 to 1.6×10^4 cm^{-3} for the most polluted case B100-E100-G100. After this, the number concentration continually decreases due to coagulation and dilution with background air.

Figure 1b shows the number fraction of BC-containing particles. For plume scenario B10-E100-G100, a scenario of high BC emission rate and low background concentration, more than 95% of all particles contain BC. On the other hand, for the plume scenario with high aerosol background and the lowest emission rate, B100-E2.5-G100, only up to 11% of particles contain BC.

The total aerosol mass concentration is shown in Figure 1c. Here we also show the total aerosol mass concentration for the G50 and the G25 plume scenarios. Note that these are run only in conjunction with the B100-E100 scenario, i.e., here we show B100-E100-G50 and B100-E100-G25. The formation of secondary

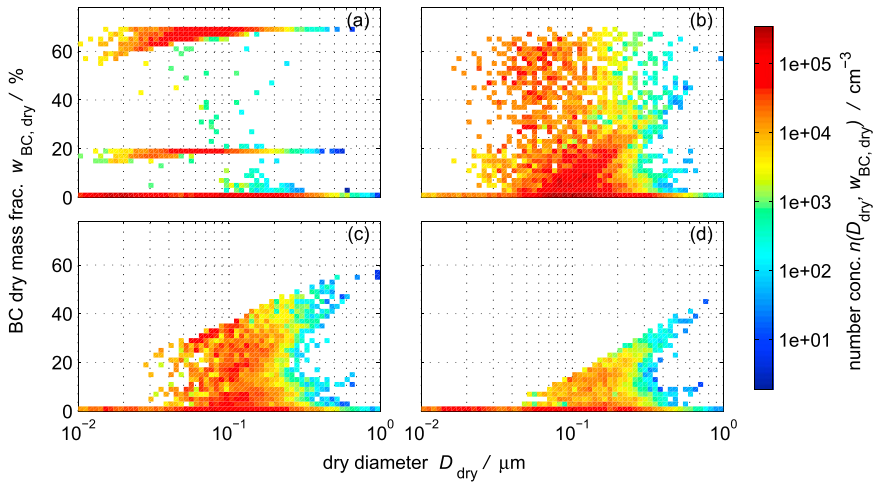

Figure 2. Two-dimensional number concentration distribution $n(D_{dry}, w_{BC,\,dry})$, at (a) $t_p = 1$ h, (b) $t_p = 12$ h, (c) $t_p = 24$ h, and (d) $t_p = 48$ h for plume scenario B100-E100-G100.

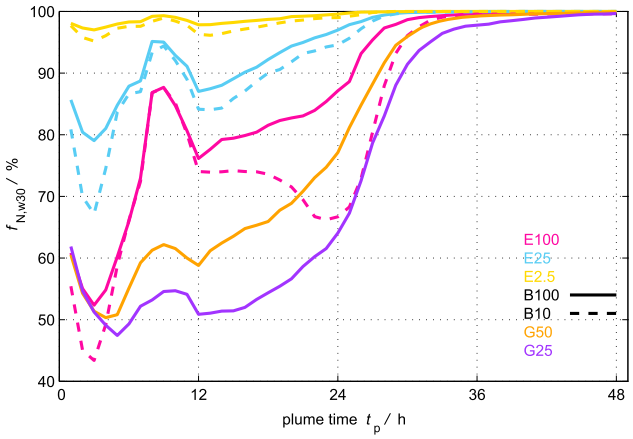

Figure 3. Fraction of particle number concentration with black carbon dry mass fraction ($w_{BC,\ dry}$) less than 30%, $f_{N,\ w30}$, as a function of plume time t_p. Magenta, blue, and yellow represent black carbon emission rate levels, E100, E25, and E2.5, respectively. Solid and dashed lines stand for background aerosol number concentrations, B100 and B10, respectively. Orange and purple solid lines represent the two plume scenarios B100-E100-G50 and B100-E100-G25, respectively.

aerosol material was similar in all G100 cases, since the emissions of gaseous precursors were the same. The total mass concentration on the first day was dominated by ammonium nitrate formation, which evaporated after ammonia emissions ceased [*Ching et al.*, 2012]. Secondary production of sulfate and organic mass also occurred on the second day of the simulation. In comparison, less secondary aerosol mass was formed in plume scenario G50 (orange line) and G25 (purple line). For example, for t_p = 12 h, m_a varies by a factor of about 2 between plume scenarios G100 and G50. The BC mass concentrations of all the plume scenarios ranged from 0.05 μg m^{-3} to 3.6 μg m^{-3} as shown in Figure 1d.

To illustrate how the BC mixing state evolved, Figure 2 shows the two-dimensional particle number concentration distribution as a function of dry diameter, D_{dry} and BC dry mass fraction, $w_{BC,\ dry}$, for plume scenario B100-E100-G100. The BC mass fraction for a particle is defined as

$$w_{BC,\,dry} = \frac{\mu^{BC}}{\mu^{dry}}, \tag{2}$$

where μ^{BC} is the particle BC mass and μ^{dry} is the particle's total dry mass. We define the two-dimensional cumulative number distribution, $N(D_{dry}, w_{BC,\,dry})$ as the number concentration of particles that have a dry diameter less than D_{dry} and a BC mass fraction less than $w_{BC,\,dry}$. We further define the two-dimensional number distribution, $n(D_{dry}, w_{BC,\ dry})$ as

$$n(D_{dry}, w_{BC,\,dry}) = \frac{\partial^2 N(D_{dry}, w_{BC,\,dry})}{\partial \log_{10} D_{dry}\, \partial w_{BC,\,dry}}. \tag{3}$$

As explained in section 3.1, we focus on four selected plume time snapshots, t_p = 1 h, 12 h, 24 h, and 48 h. These correspond to the local times of 7:00 A.M., 6:00 P.M., and 6:00 A.M. on day 2, and 66:00 A.M. on day 3. Figure 2a shows at t_p = 1 h three distinct horizontal bands representing diesel soot particles with $w_{BC,\ dry}$ = 70%, gasoline particles with $w_{BC,\ dry}$ = 20%, and meat cooking particles with $w_{BC,\ dry}$ = 0%. Background particles containing trace amounts of black carbon also contributed to the subpopulation at $w_{BC,\ dry} \approx$ 0% (see Table 1).

As the urban plume evolved over the course of the day, particles with BC dry mass fractions ranging between 70% and 0% gradually developed because of condensation of gaseous aerosol precursors and coagulation. At t_p = 12 h and thereafter, the two horizontal distinct bands at $w_{BC,\ dry}$ = 70% and $w_{BC,\ dry}$ = 20% disappeared since no fresh emissions entered the simulation. For most of the particles, $w_{BC,\ dry}$ decreased to less than 60% at t_p = 24 h and to less than 40% after 2 days. The diagonal lines appear because condensation of secondary species decreases BC mass fraction faster for smaller particles than for larger particles.

As the BC dry mass fractions of the primary particles decreased, the particles became more hygroscopic. Enhanced hygroscopicity, combined with the increase in particle sizes as a result of condensation of gaseous aerosol precursors and coagulation, led to decreases in the per-particle critical supersaturations over the course of 2 days [*Ching et al.*, 2012]. At t_p = 1 h, the freshly emitted particles' critical supersaturation ranged between 1% and 10%. After 2 days of simulation, most of the particles had critical supersaturation values less than 0.5%.

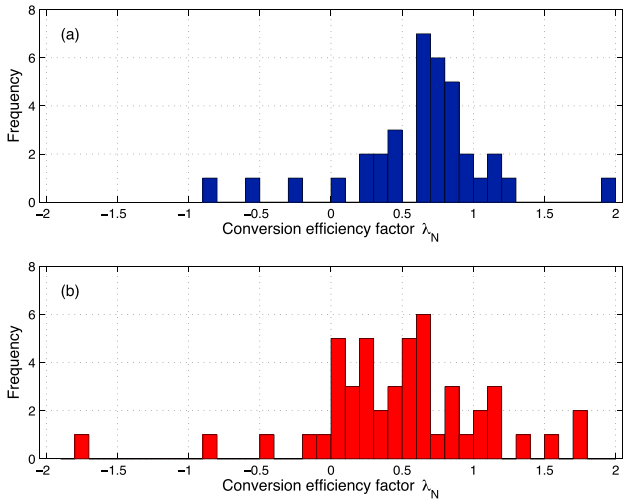

Figure 4. Frequency distribution of conversion efficiency factor λ_N, which quantifies the relative change in cloud droplet number concentration per relative change in aerosol number concentration. (a) Change in aerosol number concentration was produced by changing aerosol background concentration values. (b) Change in aerosol number concentration was produced by changing BC emission rates.

Changing the BC emission rate, background aerosol concentration or the gas emission rates impacted the per-particle composition evolution. This is summarized in Figure 3, which exemplarily shows the time evolution of the number concentration fraction of particles with $w_{BC,\ dry}$ lower than 30%, denoted $f_{N,w30}$. Given a certain plume time t_p, $f_{N,w30}$ was lower for scenarios with higher BC emission rates. For example, at $t_p = 24$ h, about 87% of particles for plume scenario B100-E100-G100 (solid magenta line) had a BC dry mass fraction of less than 30%, while for B100-E25-G100 (solid blue line), about 97%, and B100-E2.5-G100 (solid yellow line), more than 99% of all particles had BC mass fractions less than 30%. This difference arose because the plume scenarios with reduced BC emissions started out with higher values for $f_{N,w30}$. In addition, less competition existed among BC particles for condensable secondary aerosol material when BC emissions were reduced, and relatively more coagulation events occurred between BC and non-BC particles in BC emission-reduced plume scenarios (although the total number of coagulation events decreased in BC emission-reduced scenarios).

In contrast, reducing the concentration of background aerosol particles or lowering gas emission rates resulted in a slower decrease of BC mass fractions over time on a per-particle level. For example, while for B100-E100-G100 $f_{N,w30}$ increased from about 61% at $t_p = 1$ h to 87% at $t_p = 24$ h (solid magenta line), for B10-E100-G100 the corresponding change is only from 55% to 67% (dashed magenta line). Similarly, reducing the gas emission rates from G100 to G50 to G25 resulted in longer persistence of high BC dry mass fractions. For example, at $t_p = 24$ h, $f_{N,w30}$ increased from 64% to 77% and 87% as the gas phase emission rates increased from plume scenario B100-E100-G25 (solid purple line) to B100-E100-G50 (solid orange line) and B100-E100-G100 (solid magenta line).

4.2. Cloud Parcel Simulations

To evaluate how changes in the underlying aerosol population translate into changes in the cloud droplet concentration, we define the aerosol-to-cloud-droplet conversion efficiency factor λ_N as follows:

$$\lambda_N = \frac{\frac{\Delta N_d}{N_d}}{\frac{\Delta N_a}{N_a}}, \tag{4}$$

where ΔN_a is the difference in aerosol concentration between any two urban plume scenarios, and ΔN_d is the corresponding difference in cloud droplet concentration that results after performing the cloud parcel simulations. The parameter λ_N equals 1 when the relative change in aerosol concentration equals the relative change in the resulting cloud droplet concentration. A positive λ_N value indicates that ΔN_a and ΔN_d have the same sign, i.e., an increase in N_a results in an increase in N_d, and a decrease in N_a results in a decrease in N_d. When λ_N is negative, ΔN_a and ΔN_d have opposite signs, so that an increase in N_a results in a decrease in N_d and vice versa.

Figure 4 shows histograms of λ_N for all cloud parcel simulations, separated by the mechanism of how the change in aerosol concentration was produced. Figure 4a compares the urban plume scenarios with differing aerosol background concentration (B100 and B10), and Figure 4b compares the urban plume scenarios with differing BC emission rate (E100 and E25, as well as E25 and E2.5). Most of the λ_N values are positive,

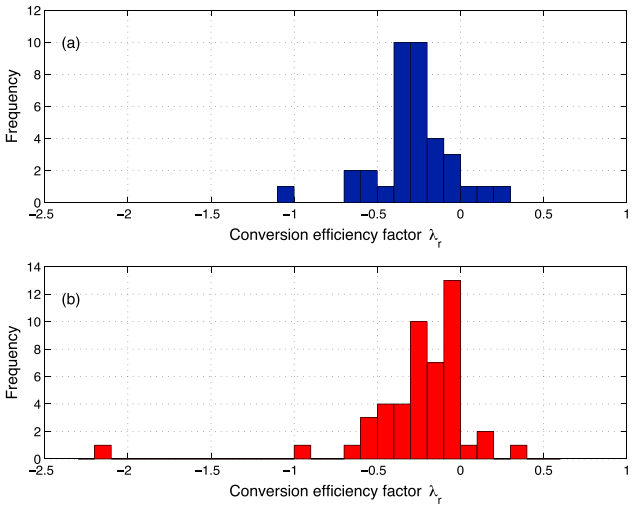

Figure 5. Frequency distribution of conversion efficiency factor λ_r, which quantifies the relative change in effective radius per relative change in aerosol number concentration. (a) Change in aerosol number concentration was produced by changing aerosol background concentration values. (b) Change in aerosol number concentration was produced by changing BC emission rates.

indicating that decreasing the aerosol background concentration or the BC emission rate does indeed result in a decrease in N_d as one might expect. However, interestingly, some cases exist where the opposite applies, represented by a negative λ_N value. We will analyze these cases in more detail in section 5.

Analogously to λ_N, we can define efficiency factors that quantify the relative in change effective radius per relative change in aerosol number concentration

$$\lambda_r = \frac{\frac{\Delta r_{eff}}{r_{eff}}}{\frac{\Delta N_a}{N_a}}, \tag{5}$$

and the relative change in relative dispersion per relative change in aerosol number concentration

$$\lambda_\epsilon = \frac{\frac{\Delta \epsilon}{\epsilon}}{\frac{\Delta N_a}{N_a}}. \tag{6}$$

The effective radius of a cloud droplet size spectrum is defined as the ratio of the third moment to the second moment of the cloud droplet spectrum. We define the cloud droplets to be particles with wet diameter greater than 2 μm, so the effective radius can be written as the following,

$$r_{eff} = \frac{\int_{1\,\mu m}^{\infty} r^3 n(r) dr}{\int_{1\,\mu m}^{\infty} r^2 n(r) dr}. \tag{7}$$

The spectral dispersion of the cloud droplet spectrum is defined as the ratio of the standard deviation of the cloud droplet spectrum to the average diameter of the droplet population,

$$\epsilon = \frac{\sigma(n(D))}{\bar{D}}. \tag{8}$$

Effective radius is an important quantity for computing cloud albedo and evaluating aerosol indirect effects [*Twomey*, 1991], and relative dispersion is needed to accurately parameterize effective radius [*Martin et al.*, 1994; *McFarquhar and Heymsfield*, 2001; *Liu and Daum*, 2000, 2002], evaluate the aerosol indirect effect [*Rotstayn and Liu*, 2003], and parameterize autoconversion rates [*Liu and Daum*, 2004].

Figure 5 shows that most values for λ_r are negative, which is consistent with the fact that in most cases an increase in aerosol particle number concentration leads to a higher cloud droplet number concentration, but smaller cloud droplets. The response in relative dispersion shown in Figure 6 is not as straightforward to interpret but is consistent with the work by *Chen et al.* [2016]. They defined two different regimes for aerosol-cloud interactions based on the response of ϵ to increases in aerosol number concentration. Given a certain updraft velocity, the aerosol-limited regime is characterized by increasing ϵ with increasing N_a (positive λ_r), while the updraft-limited regime is characterized by decreasing ϵ with increasing N_a (negative λ_r). Since most of our λ_ϵ values are positive, we conclude that our simulations cover mostly the aerosol-limited regime.

To further evaluate how differences in CCN properties of the underlying aerosol population translate to the corresponding differences in cloud droplet number concentration, the maximum saturation ratio, S_{max}, attained in the parcel simulation is the critical factor, which in turn depends on aerosol population properties and the cloud parcel cooling rate. In the next section, we will examine how the difference in N_d for any

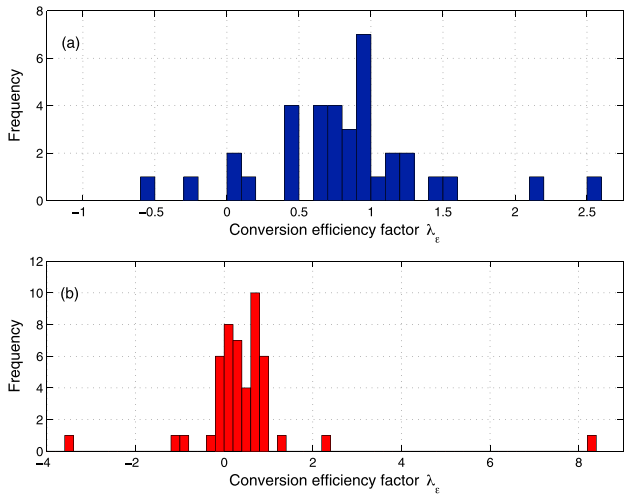

Figure 6. Frequency distribution of conversion efficiency factor λ_ϵ, which quantifies the relative change in relative dispersion per relative change in aerosol number concentration. (a) Change in aerosol number concentration was produced by changing aerosol background concentration values. (b) Change in aerosol number concentration was produced by changing BC emission rates.

two cloud parcel simulations can be attributed to changes in the plume properties and changes in the cloud parcel response.

5. Plume Effect and Parcel Effect

Changing BC emission rates, the aerosol background concentration or gas emission rates can modify the aerosol CCN spectrum in the urban plume. However, given a certain cooling rate, this only partially explains the subsequent change in cloud droplet number concentration, because the maximum saturation ratio in the cloud parcel changes also in response to the altered aerosol population. In this section we develop a framework to disentangle these two factors, so that we can attribute differences in cloud droplet number concentration between two cloud parcel simulations to differences in the underlying aerosol population ("plume effect") and to differences in the maximum saturation ratio response ("parcel effect"). We then apply the framework to compare cloud parcel simulations with different aerosol background concentration and with different black carbon emission rates. For this paper we are especially interested in relating the findings to black carbon mixing state.

To attribute the differences in cloud droplet number concentration between any two cloud parcel simulations to the differences in the corresponding CCN spectra of the underlying aerosol populations and to the maximum supersaturation achieved in the parcel simulations, we introduce the quantities shown schematically in Figure 7. The two CCN spectra correspond to aerosol populations from two different urban plume scenarios. When used as input for the cloud parcel simulations the maximum supersaturations $s_{max,1}$ and $s_{max,2}$, respectively, are reached. The intersections with the CCN spectra represent the resulting cloud droplet number concentrations, $N_{d,1}$ and $N_{d,2}$ assuming that particles with critical supersaturation lower than s_{max} become cloud droplets, which neglects the impact of kinetic limitation [*Nenes et al.*, 2001]. Kinetic limitation is accounted for in our cloud parcel simulations and is not negligible; hence, using s_{max} would overestimate the cloud droplet concentrations.

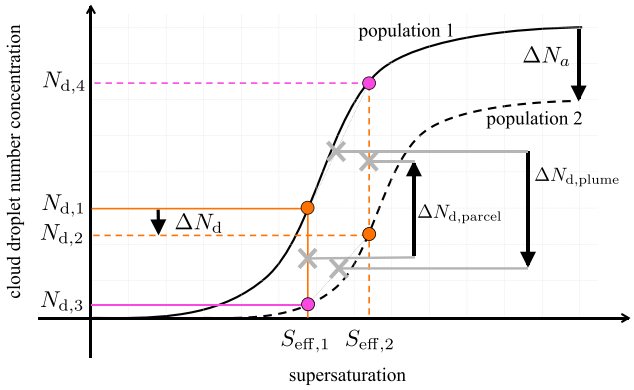

Figure 7. Illustration of plume and parcel effects to attribute change in cloud droplet number concentration (ΔN_d) when comparing two different scenarios. In this case the total aerosol concentration was reduced (ΔN_a), which resulted in a net reduction of the cloud droplet number concentration (ΔN_d). This reduction is a superposition of a large decrease in CCN concentrations ($\Delta N_{d,plume}$) combined with an increase of supersaturation in the cloud parcel ($\Delta N_{d,parcel}$).

We can circumvent this problem since, at the end of the cloud parcel simulation, we know exactly which aerosol particles end up as cloud droplets and which ones remain as interstitial particles, after the transient activation process is over. Specifically, we know the maximum critical supersaturation of the particles that were able to form cloud droplets (s_1). These are the particles that "just made it" to become cloud droplets. All particles with critical

supersaturation lower than s_1 will also form cloud droplets. We also know the minimum critical supersaturation of the particles that remained interstitial particles (s_2). These are the particles that "just did not make it" to become cloud droplets. All particles with critical supersaturation higher than s_2 will also remain interstitial particles. Importantly, $s_1 < s_2 < s_{max}$ if kinetic limitation is present. The threshold value of supersaturation that separates the cloud droplet population from the interstitial aerosol population is therefore between s_1 and s_2. We estimate this value by taking the average of s_1 and s_2 and call this the "effective supersaturation" s_{eff}, and we use s_{eff} to determine $N_{d,1}$ and $N_{d,2}$ from the CCN spectra. In practice s_1 and s_2 are very close, and they are both lower than s_{max}.

To decompose the difference in cloud droplet number concentration between two cloud parcel simulations, $\Delta N_d = N_{d,2} - N_{d,1}$, into a plume and a parcel component, it is useful to define $N_{d,3}$ as the cloud droplet number concentration for cloud parcel simulation 2 if the effective supersaturation attained was $s_{eff,1}$, and $N_{d,4}$ as the cloud droplet number concentration for cloud parcel simulation 1 if the maximum supersaturation was $s_{eff,2}$. We then rewrite ΔN_d:

$$\begin{aligned}\Delta N_d &= N_{d,2} - N_{d,1} \\ &= \frac{1}{2}\left(N_{d,2} - N_{d,3} + N_{d,3} - N_{d,1}\right) + \frac{1}{2}\left(N_{d,2} - N_{d,4} + N_{d,4} - N_{d,1}\right) \\ &= \underbrace{\frac{1}{2}\left(N_{d,2} + N_{d,3}\right) - \frac{1}{2}\left(N_{d,1} + N_{d,4}\right)}_{\Delta N_{d,\,plume}} + \underbrace{\frac{1}{2}\left(N_{d,2} + N_{d,4}\right) - \frac{1}{2}\left(N_{d,1} + N_{d,3}\right)}_{\Delta N_{d,\,parcel}}\end{aligned} \tag{9}$$

As seen in Figure 7, $\Delta N_{d,\,plume}$ can be understood as the difference in N_d calculated using the CCN spectra of urban plume scenarios 1 and 2 at the average of $s_{eff,1}$ and $s_{eff,2}$. Similarly, $\Delta N_{d,\,parcel}$ is the difference in N_d calculated with an averaged CCN spectrum of the two scenarios at $s_{eff,1}$ and $s_{eff,2}$.

We then can express the conversion efficiency factor λ_N as the sum of a plume component and a parcel component:

$$\lambda_N = \frac{\frac{\Delta N_{d,plume}}{N_d}}{\frac{\Delta N_a}{N_a}} + \frac{\frac{\Delta N_{d,parcel}}{N_d}}{\frac{\Delta N_a}{N_a}}, \tag{10}$$

$$\lambda_N = \lambda_{N,plume} + \lambda_{N,parcel}. \tag{11}$$

We can map the cloud parcel simulation results in the two-dimensional space formed by $\lambda_{N,parcel}$ and $\lambda_{N,plume}$ as shown in Figure 8. For points in quadrants 2 and 4 the plume and parcel effect counteract each other, which exemplifies the buffering mechanism in the cloud droplet formation process [*Stevens and Feingold*, 2009; *Carslaw et al.*, 2013]. For points in quadrants 1 and 3 the plume and parcel effect reinforce each other. The diagonal with slope −1 indicates $\lambda_N = 0$. Points along this line show no change in cloud droplet number concentrations, even though the plume and parcel effects can be large individually.

Points from the simulations where the aerosol background concentration was changed are shown in blue, corresponding to Figure 4a. For all these cases $\lambda_{N,plume}$ is positive and $\lambda_{N,parcel}$ negative. The effective supersaturation for the B10 simulations reached higher values than for the B100 simulations due to reduced water vapor competition when less background aerosol particles are present. For most cases the magnitude of $\lambda_{N,plume}$ was larger than the magnitude of $\lambda_{N,parcel}$. This means that the differences in cloud droplet number concentration when changing the aerosol background concentration were mainly due to changes in the aerosol population. Three exceptions exist where the magnitude of $\lambda_{N,parcel}$ was larger than that of $\lambda_{N,plume}$ For these three cases a reduction from B100 to B10 led to an increase in cloud droplet number concentration, because the increase in supersaturation overcompensated the decrease in CCN concentration. These were the cases from the cloud parcel simulations using urban plume scenarios B100-E100-G100-T12 and B10-E100-G100-T12 (all three cooling rates). The scenario B100-E100-G100-T12 had the highest aerosol number concentration (see Figure 1a), and most particles were aged and CCN active. Although the total number concentration decreased when reducing the background concentration from B100 to B10, the reduced competition of water vapor in the B10 scenario led to an increase in effective supersaturation that caused more particles to activate than in B100.

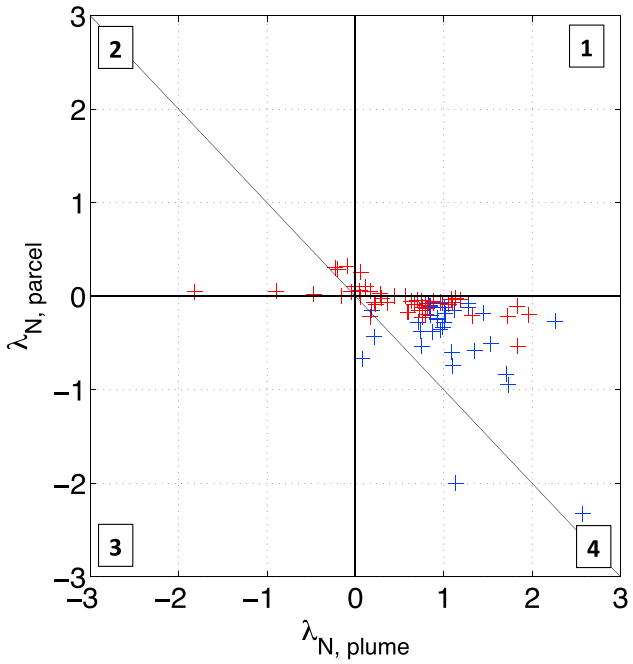

Figure 8. Plume and parcel component of the conversion efficiency factor λ_N. Points above the diagonal line correspond to a net-positive λ_N. Blue symbols correspond to the cases when the change in aerosol number concentration was produced by changing aerosol background concentration values (compare to Figure 4a). Red symbols correspond to cases when the change in aerosol number concentration was produced by changing BC emission rates (compare to Figure 4b).

Points from the simulations where different BC emission rates were compared are shown in red, corresponding to Figure 4b. These illustrate two different effects of BC on clouds, which we termed the "additive" effect and the "competition" effect. The values for $\lambda_{N,plume}$ are positive in most cases, i.e., reducing BC emissions resulted in reduced CCN concentrations, combined with a negative value of $\lambda_{N,parcel}$. This indicates that a similar mechanism operates here as discussed for the cases when the aerosol background concentration changed. Since under these conditions emitting more BC particles will increase CCN concentrations, we refer to this as the additive effect. In *Bond et al.* [2013, section 7.2, Figure 24] this is called the LC1 effect. Noteable exceptions from this pattern are four cases with negative values for $\lambda_{N,plume}$. For these cases the reduction in BC emissions led to more CCN. A common feature of these cases is that they were all based on T1-urban plume scenarios and contained therefore mainly fresh BC particles. Reducing the concentration of these particles reduced the competition of BC particles for secondary aerosol material, leading to overall more CCN, and we refer to this as the competition effect. This is similar, but not identical, to the LC2 effect mentioned in *Bond et al.* [2013, section 7.2, Figure 24]. The LC2 effect assumes that by reducing BC, sulfate might preferentially form fresh particles and additional sulfate would condense upon pure sulfate particles, thereby resulting in more CCN; however, those CCN do not contain BC. In our cases we observe the competition for condensable material among the BC particles.

A few data points fall in the first quadrant indicating that the plume and the parcel effect reinforce each other. However, the magnitudes of both $\lambda_{N,plume}$ and $\lambda_{N,parcel}$ are small, and we therefore do not consider these cases further.

6. Error in Cloud Microphysical Properties Due to Simplified Aerosol Mixing State Representation

To quantify the importance of aerosol mixing state for predicting cloud microphysical quantities, we compared the particle-resolved cloud parcel simulations as presented in section 4 to simulations where we averaged the composition of the input aerosol population within prescribed size bins before performing the cloud parcel simulation.

Ching et al. [2012, Appendix B] both presented a procedure to average particles to force them to have the same composition and derived the conservation properties of this averaging algorithm. Here we generalized this approach to apply it to the simulations that use the weighted flow algorithm [*DeVille et al.*, 2011]. We explain the details of the new procedure in Appendix A. The particles are placed in 25 logarithmically spaced size bins ranging from 10^{-10} to 10^{-5} m according to their dry diameters. In each size bin, the particles are averaged to have the same composition, but they retain their original sizes.

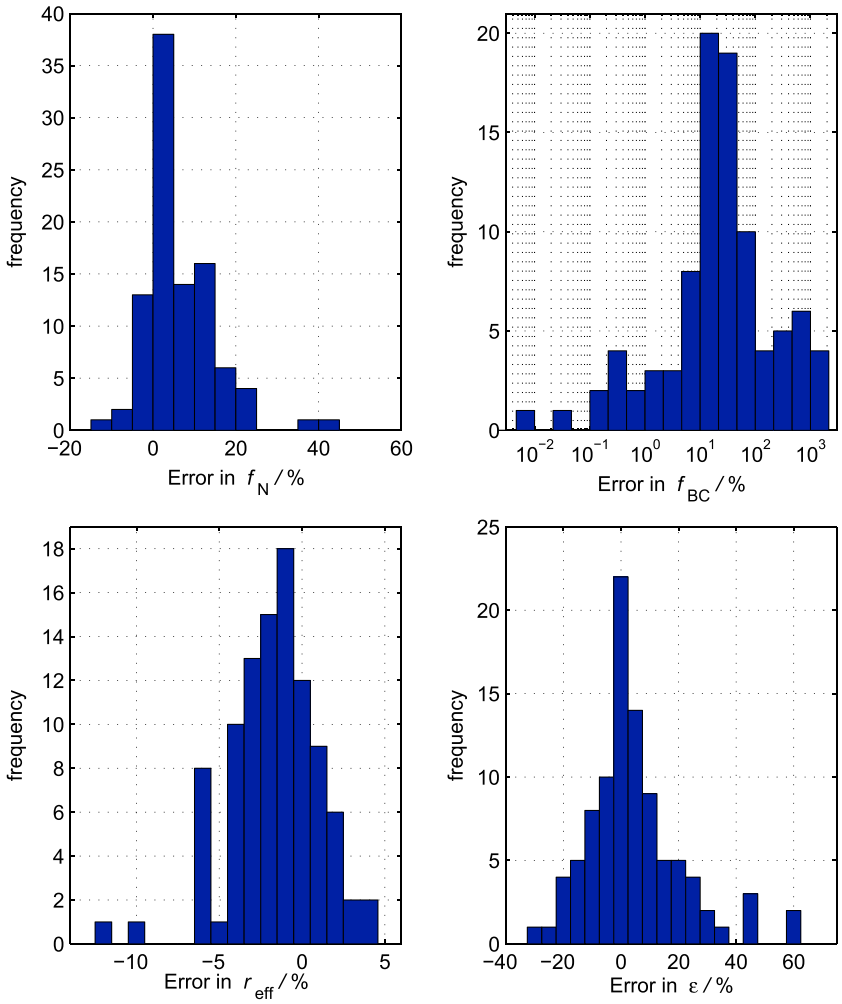

Figure 9. Frequency distributions of the error in the four cloud microphysical quantities, f_N, f_{BC}, r_{eff} and ϵ, due to composition averaging. Note that the bins for f_{BC} are logarithmically spaced.

We constructed such a "composition-averaged" cloud parcel input from all urban plume scenarios and evaluated the differences between particle-resolved reference case and composition-averaged case for four cloud microphysical quantities, namely, cloud droplet number fraction f_N, mass fraction of BC that is nucleation-scavenged f_{BC}, effective radius r_{eff}, and relative spectral dispersion ϵ.

We define the error for a quantity X due to composition averaging as

$$\Delta X = \frac{X_{comp} - X_{ref}}{X_{ref}}, \tag{12}$$

where X_{comp} and X_{ref} are values of quantity X calculated with composition-averaged and particle-resolved aerosol population, respectively, and X can be f_N, f_{BC}, r_{eff}, or ϵ.

Figure 9 shows histograms of the frequency distribution of the errors in the four quantities, f_N, f_{BC}, r_{eff}, and ϵ for all 96 cloud parcel simulations. For the cases investigated, Δf_N was within 25%, with overestimations more prevalent. One cloud parcel simulation produced an error outside this range ($\Delta f_N \sim 45\%$ for B10-E100-G100-T1-C0.5), since it contained very diverse externally mixed hydrophobic and hygroscopic subpopulations as explained in more detail below. The error in scavenged BC mass concentration can be as large as several hundred percent and consists exclusively of overpredictions. Simplified aerosol mixing state representation can result in both underprediction and overprediction of spectral dispersion, with the magnitude ranging between −30% and +60%.

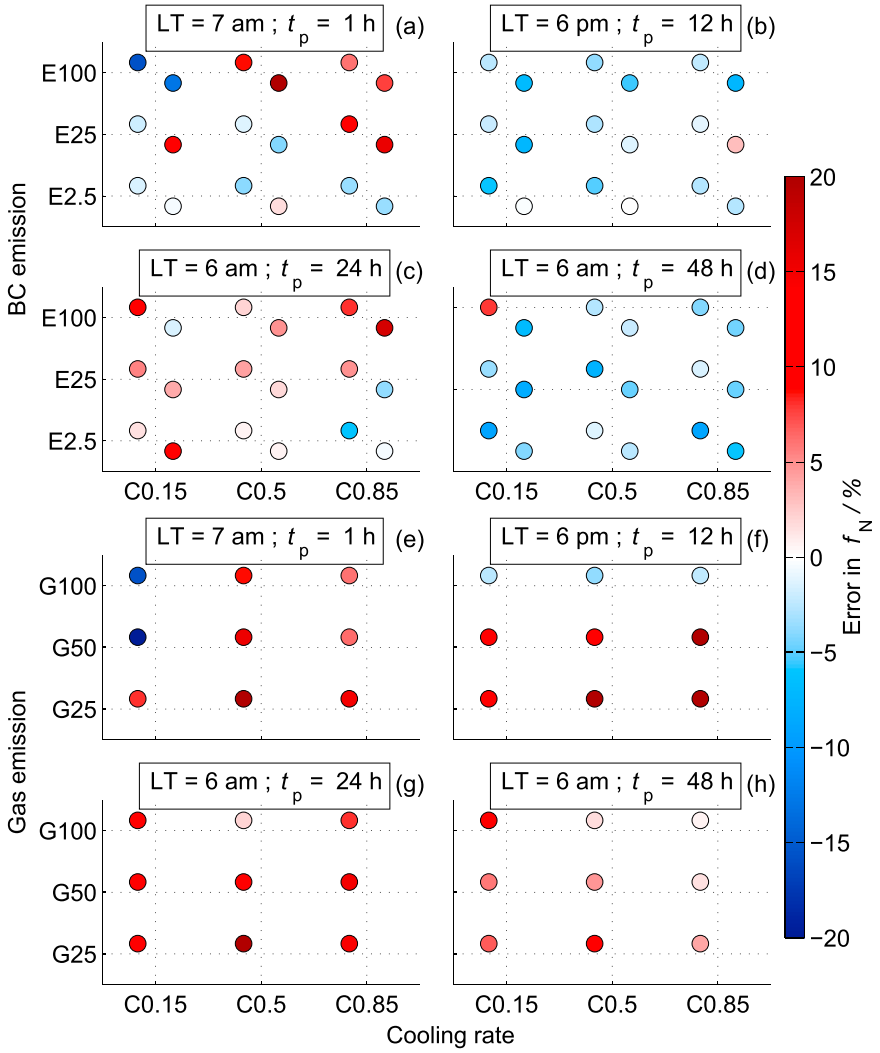

Figure 10. Error in activation fraction, f_N, due to composition averaging as a function of BC emission rate and cooling rate (a–d) and as a function of gas emission rate and cooling rate (e–f). The two dots next to each other for each BC emission rate and cooling rate (a–d) represent the results for the B100-scenario (upper left symbol) and the B10-scenario (lower right symbol). To increase the color resolution of the color bar, the maximum error was capped at 20%. The maximum error in f_N is 45% and occurs for B10-E100-G100-C0.5-T1.

Composition averaging resulted in an underprediction of the effective radius r_{eff} for most of the cloud parcel simulations. The underprediction in r_{eff} is consistent with the overprediction in f_N, and the magnitudes of Δr_{eff} are approximately 1/3 of the corresponding magnitudes of Δf_N (see *Ching et al.* [2012] for the derivation), with a range between +4.6% and −12.3%.

The errors in f_N (and therefore also in r_{eff}) and f_{BC} depend in a systematic way on some of the input parameters. To visualize this, we display the results as shown in Figures 10 and 11. The upper four panels, (Figures 10a–10d and 11a–11d), show the error for the quantity of interest for all G100 plume scenarios as a function of cooling rate (abscissa) and BC emission rate (ordinate) at four selected plume hours, t_p = 1 h, t_p = 12 h, t_p = 24 h, and t_p = 48 h, respectively. The two simulations at different levels of aerosol background concentrations for the same BC emission rate and cooling rate are shown by two dots next to each other, with the upper left symbol for B100 and the lower right symbol for B10. The lower four panels, (Figures 10e–10h and 11e–11h), show the error for the B100-E100 plume scenarios, now stratified by cooling rate and gas emission rate, for the same four selected plume hours.

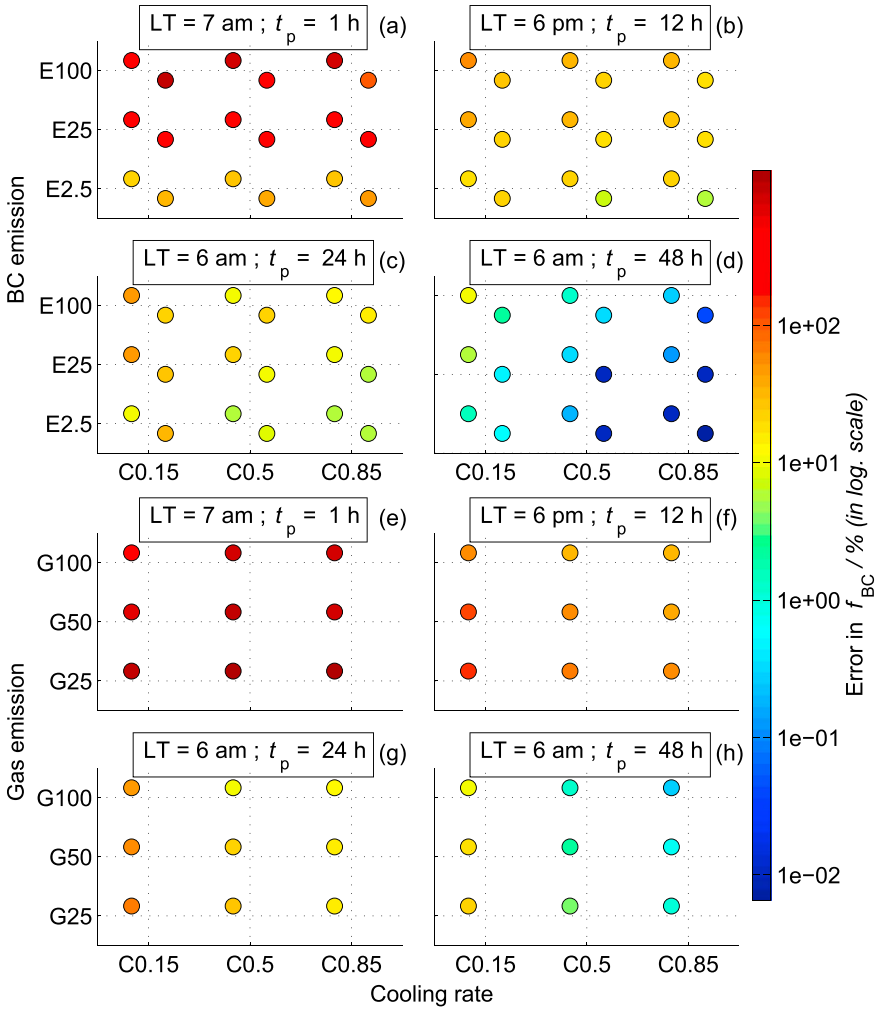

Figure 11. Error in black carbon nucleation-scavenged fraction, f_{BC}, due to composition averaging as a function of BC emission rate and cooling rate (a–d), and as a function of gas emission rate and cooling rate (e–f). The two dots next to each other for each BC emission rate and cooling rate (a–d) represent the results for the B100-scenario (upper left symbol) and the B10-scenario (lower right symbol). Note the logarithmic scale of the color bar.

Figure 10 shows that comparing the four different plume times, the overestimation in f_N is largest for t_p = 1 h, reaching a maximum of 45% for B10-E100-G100-T1-C0.5. At this time the population consists of two distinct subpopulations, namely, freshly emitted hydrophobic black carbon particles and hygroscopic background particles, as shown in Figure 2a. Composition averaging results in an artificial mixing of hydrophobic and hygroscopic aerosol material. After this procedure some aerosol particles can activate that would not activate in the particle-resolved reference calculation, and vice versa. The net outcome for most conditions simulated here is that f_N increases after composition averaging, giving rise to positive Δf_N. For some cases, f_N decreases after composition averaging, leading to negative Δf_N. These are cases for early plume hours when the subpopulation of BC particles is still fresh.

At later plume hours (Figures 10b–10d), some aging of the BC-containing particles has taken place, and the artificial mixing has less impact on N_d; hence, Δf_N decreases. However, the details of this aging process in the urban plume play a role. For example, at t_p = 24 h, the errors in f_N are larger than at t_p = 12 h and 48 h. This is due to evaporation of ammonium nitrate toward the end of the first day, reversing the aging process to some extent [*Ching et al.*, 2012, Figure 1d].

Figures 10e–10h show that the errors in f_N for the G50 and G25 plume scenarios are larger than that for the G100 simulations. The maximum error in f_N was 11% among all B100-E100 plume scenarios at G100, while it reached 22% and 25% for G50 and G25, respectively. When the gas emission rates are reduced,

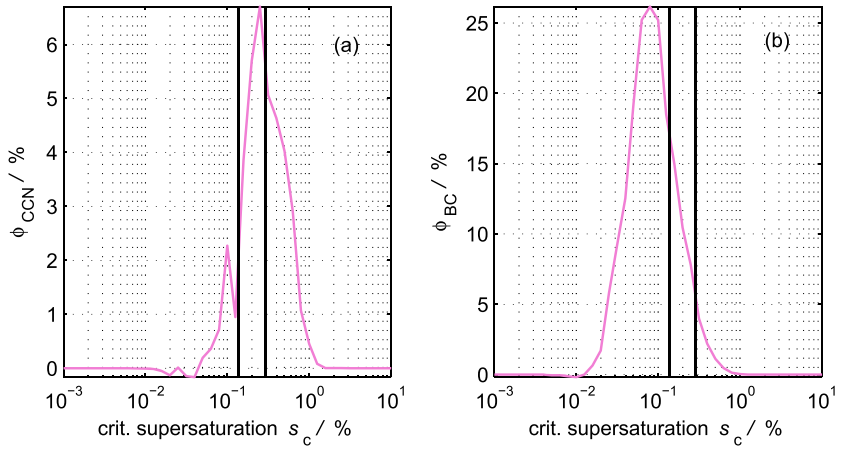

Figure 12. (a) Difference in CCN concentration fraction between particle-resolved and composition-averaged calculations, ϕ_{CCN}; (b) difference in BC mass concentration fraction, ϕ_{BC} as a function of critical supersaturation, s_c for scenario B100-E25-G100-T24. The two vertical lines indicate the maximum supersaturations attained in cloud parcel simulations at two cooling rates, C0.15 (the left vertical line in each panel) and C0.85 (the right vertical line in each panel).

less condensable secondary aerosol mass is produced, so the aerosol aging process is slowed down, and larger errors persist for a comparatively longer time. From the overview in Figure 10 it also becomes obvious that Δf_N does not show any simple relationship with cooling rate, black carbon emission rate or background particle concentration.

Figure 11 show the errors in nucleation-scavenged BC mass fraction. Note that the color bar is scaled logarithmically. The errors, Δf_{BC}, are largest for $t_p = 1$ h, ranging between 21% and 1022%, and gradually decrease for larger plume times. For example, at $t_p = 12$ h, Δf_{BC} lies in a much smaller range, from 6% to 58%. Similar to Δf_N and for the same reasons, Δf_{BC} increases for the simulations with reduced gas phase emissions.

Comparing the magnitudes of Δf_N to Δf_{BC}, we see that small error in f_N does not necessarily imply small error in f_{BC}, and this is again consistent with the findings in *Ching et al.* [2012]. The reason is that composition averaging distorts the mixing state information. Even if the cloud droplet number concentrations are the same in particle-resolved and composition-averaged calculations, the composition of the particles may differ substantially, which leads to larger errors in Δf_{BC}. This study confirms that this holds true in an extended parameter space of BC emission rate, background particle concentration, gas emission rate, and cooling rate.

It is interesting to note that Δf_{BC} decreases for increasing cooling rate, while for Δf_N we do not see a systematic dependence on cooling rate. To explain this, we compare the dependence on supersaturation of the following two quantities:

$$\phi_{CCN} = \left(\frac{N_{CCN}}{N_a}\right)_{comp} - \left(\frac{N_{CCN}}{N_a}\right)_{ref}$$

$$\phi_{BC} = \left(\frac{m_{BC}}{m_a}\right)_{comp} - \left(\frac{m_{BC}}{m_a}\right)_{ref},$$

where N_{CCN} is the CCN number concentration at a given supersaturation, and m_{BC} is the black carbon mass concentration associated with the corresponding CCN population. N_a and m_a are total number and mass concentration, respectively. The subscripts "comp" and "ref" denote whether the calculation is based on composition-averaged or particle-resolved population. The quantities ϕ_{CCN} and ϕ_{BC} as a function of supersaturation show how Δf_N and Δf_{BC} vary with cooling rate (or cloud parcel supersaturation).

Figure 12 depicts ϕ_{CCN} and ϕ_{BC} for the cloud parcel simulation using input B100-E25-G100-T24 (upper row for E25 in Figures 10c and Figure 11c), but this is representative for all the cloud parcel simulations considered here. The black vertical lines represent the two maximum supersaturations that were attained in the cloud parcel simulations for the lowest and the highest cooling rate, C0.15 and C0.85, respectively.

Both ϕ_{CCN} and ϕ_{BC} are zero for very small and very high supersaturations. This is expected, since for very low ambient supersaturations none of the particles activate, while for very high ambient supersaturations all particles activate, regardless of the per-particle composition. A maximum in ϕ_{CCN} and ϕ_{BC} is obtained for intermediate supersaturation values. It turns out that the maximum of ϕ_{BC} (or Δf_{BC}) is reached for lower ambient supersaturations compared to ϕ_{CCN} (or Δf_N). The maximum supersaturations attained in the cloud parcels intersect the ϕ_{BC} curve on the right shoulder; hence, higher cooling rates consistently result in smaller Δf_{BC}. In contrast, the ϕ_{CCN} curve is intersected on the left shoulder or (for some other examples) around the maximum of the curve. Hence, Δf_N can increase or decrease with increasing cooling rate.

7. Summary and Conclusion

We constructed the first-ever set of particle-resolved cloud parcel simulations covering a range of realistic conditions to study two different impacts of BC mixing state on cloud formation: (1) how does BC mixing state affect the change in cloud droplet number concentration caused by a change in aerosol number concentration and (2) if we neglect BC mixing state information, how much error is incurred in cloud microphysical properties?

In section 5, we developed a new process-level analysis method to attribute the response in cloud droplet number concentration to changes in the underlying aerosol population ("plume effect") and to changes in the attained maximum supersaturation in cloud parcel ("parcel effect"). We applied this method to about 100 cloud parcel simulations, which differed in their underlying initial aerosol population and in the cooling rate that they experienced. In most of the simulations the plume and parcel effect had opposite signs, with the plume effect dominating.

The results quantify the magnitudes for two different effects of BC on clouds, the "additive effect" and the "competition effect." Depending on which of these two effects prevails, emitting BC particles may result in either more or less CCN overall. We quantified the conditions under which each of these effects dominates and showed that this depends on the BC mixing state. The additive effect dominates when aged BC particles are present, which then form cloud droplets readily. An increase in BC emissions will result in an increase of cloud droplet number concentration. In contrast, the competition effect dominates when the BC particles in the population are fresh, and an increase in BC emissions will result in a decrease of cloud droplet number concentration. In the cloud parcel simulations considered here the additive effect was more prevalent, as BC particles aged fairly quickly in the evolving urban plumes. Translating this to the real atmosphere, we would expect to find the competition effect acting only close to the emission sources, and models would need to resolve mixing state to capture the transition from the competition regime to the additive regime.

In section 6, we computed the first quantification of the errors in cloud microphysical properties that result from neglecting per-particle composition information over a range of scenarios. The error ranged from −12% to +45% for the fraction of aerosol particles that activated to form cloud droplets, and from −12% to +4% for the cloud droplet effective radius. The errors in the spectral dispersion ranged from −30% to +60% for the scenarios investigated here. These errors are smaller than the enhancement in spectral dispersion caused by entrainment, which can widen cloud droplet spectra by an order of magnitude [*Bewley and Lasher-Trapp*, 2011]. The nucleation-scavenged BC mass fraction can be overestimated by over 1000%. Errors in activation fraction, effective radius, and scavenged BC mass fraction tended to be larger for the scenarios that contained a subpopulation of fresh BC particles, which were artificially aged by the composition-averaging procedure. This was the case for the scenarios at early plume times (representing conditions close to emission sources), and for scenarios with reduced gas emission rate, since for these scenarios less secondary aerosol mass was produced; hence, the aging process was slowed down. As found in *Ching et al.* [2012] a small error for activation fraction was not necessarily associated with a small error for scavenged BC mass fraction. In contrast to the error in activation fraction, the error in nucleation-scavenged mass fraction showed a decrease with increasing cooling rate.

Slingo [1990] suggested that examining cloud impacts on climate requires an accuracy of 5% in cloud microphysical quantities such as cloud droplet number concentration and effective radius of cloud droplets. Similarly, *Ohring et al.* [2005] recommended an accuracy of 2% to 10% for cloud droplet effective radius. Our results show that neglecting aerosol mixing state by itself can produce errors of this magnitude.

Appendix A: Weighted Averaging

As discussed in section 6, the averaging procedures originally developed in *Ching et al.* [2012, Appendix B] do not directly apply to the weighted flow algorithm [*DeVille et al.*, 2011] used in this paper. In this appendix we describe how to extend the averaging procedures to this case. In the following subsections we consider a single-size bin containing N particles. To extend these procedures to an entire particle population the averaging is done independently for the set of particles in each bin.

Section A1 extends composition averaging to the weighted case and shows that all properties of the unweighted algorithm carry over. Unlike composition averaging, size averaging cannot be extended to the weighted case while preserving all bulk quantities (total volume/mass and total number). Instead, we present two variants of the size-averaging procedure, one that preserves total volume or mass and one that preserves total number. Sections A2 and A4 present these two variants and show that in general the combination of composition averaging and size averaging still cannot preserve both total volume/mass and total number, although there a correction can be applied in the single-bin case to achieve this outcome.

A1. Composition Averaging

Composition averaging takes the N particles in each bin and gives them each the same composition (i.e., the same volume fractions of constituent species) while preserving the individual particle sizes and the total bulk species volume fractions. The results can be extended to mass fractions by multiplying the volumes by the appropriate species densities.

We begin by defining the basic quantities:

$$v_i^a = \text{ volume of species } a = 1, \dots, A \text{ in particle } i = 1, \dots, N \tag{A1}$$

$$W(v) = \text{ weighting function at volume } v. \tag{A2}$$

From these basic quantities we can define several derived quantities:

$$v_i = \sum_{a=1}^{A} v_i^a = \text{ total volume of particle } i \tag{A3}$$

$$v_W^a = \sum_{i=1}^{N} W(v_i) v_i^a = \text{ weighted total volume of species } a \text{ in all particles} \tag{A4}$$

$$v_W = \sum_{i=1}^{N} \sum_{a=1}^{A} W(v_i) v_i^a = \sum_{i=1}^{N} W(v_i) v_i = \sum_{a=1}^{A} v_W^a = \text{ weighted total volume of all particles} \tag{A5}$$

$$N_W = \sum_{i=1}^{N} W(v_i) = \text{weighted total number.} \tag{A6}$$

The weighted composition-averaged particles are specified by their species volumes $\tilde{v}_i^a$, defined by

$$\tilde{v}_i^a = \frac{v_W^a v_i}{v_W}. \tag{A7}$$

From the above definition, we can derive the following properties of weighted composition averaging:

$$\tilde{v}_i = \sum_{a=1}^{A} \tilde{v}_i^a = \sum_{a=1}^{A} \frac{v_W^a v_i}{v_W} = v_i \text{ (particle volumes are preserved)} \tag{A8}$$

$$\tilde{v}_W^a = \sum_{i=1}^{N} W(\tilde{v}_i) \tilde{v}_i^a = \sum_{i=1}^{N} W(v_i) \frac{v_W^a v_i}{v_W} = v_W^a \quad \text{(weighted total species volumes are preserved)} \tag{A9}$$

$$\tilde{v}_W = \sum_{i=1}^{N} \sum_{a=1}^{A} W(\tilde{v}_i) \tilde{v}_i^a = \sum_{i=1}^{N} \sum_{a=1}^{A} W(v_i) \frac{v_W^a v_i}{v_W} = \sum_{i=1}^{N} W(v_i) v_i = v_W \quad \text{(weighted total volume is preserved)} \tag{A10}$$

$$\tilde{N}_W = \sum_{i=1}^{N} W(\tilde{v}_i) = \sum_{i=1}^{N} W(v_i) = N_W \text{ (weighted total number is preserved)} \tag{A11}$$

$$\frac{\tilde{v}_i^a}{\tilde{v}_i} = \frac{v_W^a v_i}{v_W}\frac{1}{v_i} = \frac{v_W^a}{v_W} \quad \text{(per-particle species ratios are all equal to the weighted total species ratios)} \tag{A12}$$

$$\frac{\tilde{v}_i}{\tilde{v}_W} = \frac{v_i}{v_W} \text{ (particle volume ratios of weighted total volume are preserved).} \tag{A13}$$

From the above results we see that weighted composition averaging preserves the same properties as the original (unweighted) composition-averaging procedure [*Ching et al.*, 2012, Appendix B1].

A2. Size Averaging (Volume- or Mass-Preserving Version)

Size averaging takes the N particles in each bin and gives each of them the same size (i.e., the same volume) while preserving the per-particle compositions (i.e., the volume fractions of constituent species). We present the volume-preserving version here and the mass-preserving version using constituent masses rather than constituent volumes.

We use the notation from section A1. The weighted size-averaged particles (volume-preserving version) are specified by their species volumes $\check{v}_i^a$, which are defined by

$$\check{v}_i^a = \frac{v_i^a}{v_i} v^*, \tag{A14}$$

where v^* satisfies

$$v_W = \sum_{i=1}^{N} W(v_i) v_i = \sum_{i=1}^{M} W(v^*) v^*. \tag{A15}$$

If W is continuous then at least one v^* exists in $\left[\min_{i=1}^{N}(v_i), \max_{i=1}^{N}(v_i)\right]$. If $vW(v)$ is also strictly monotonic (as is the case for the weighting schemes used in this paper) then v^* is unique.

From the above definition we obtain the following properties of weighted size averaging (volume-preserving version):

$$\check{v}_i = \sum_{a=1}^{A} \check{v}_i^a = \sum_{a=1}^{A} \frac{v_i^a}{v_i} v^* = v^* \quad \text{(particle volumes are weighted-average volume)} \tag{A16}$$

$$\check{v}_W^a = \sum_{i=1}^{N} W(\check{v}_i)\check{v}_i^a = \sum_{i=1}^{N} W(v^*)\frac{v_i^a}{v_i} v^* \neq v_W^a \quad \text{(weighted total species volumes are not preserved)} \tag{A17}$$

$$\check{v}_W = \sum_{i=1}^{N}\sum_{a=1}^{A} W(\check{v}_i)\check{v}_i^a = \sum_{i=1}^{N}\sum_{a=1}^{A} W(v^*)\frac{v_i^a}{v_i} v^* = \sum_{i=1}^{N} W(v^*) v^* = v_W \text{ (weighted total volume is preserved)} \tag{A18}$$

$$\check{N}_W = \sum_{i=1}^{N} W(\check{v}_i) = \sum_{i=1}^{N} W(v^*) \neq N_W \quad \text{(weighted total number is not preserved)} \tag{A19}$$

$$\frac{\check{v}_i^a}{\check{v}_i} = \frac{\frac{v_i^a}{v_i} v^*}{v^*} = \frac{v_i^a}{v_i} \text{ (per-particle species ratios are preserved)} \tag{A20}$$

$$\frac{\check{v}_i}{\check{v}_W} = \frac{v^*}{v_W} \text{ (particle volume ratios of total volume are all equal).} \tag{A21}$$

Here we see that size averaging (volume-preserving version) does indeed preserve the total volume as well as the per-particle compositions, but that total species volumes and total number are not preserved.

A3. Combining Size and Composition Averaging (Volume- or Mass-Preserving Version)

Combining both volume-preserving size and composition averaging retains the above preservation properties from section A2 and additionally preserves total species volumes. To see this, we calculate the particle compositions $\check{v}_i^a$ resulting from doing weighted size averaging after weighted composition averaging:

$$\check{v}_i^a = \frac{\tilde{v}_i^a}{\tilde{v}_i}\tilde{v}^* = \frac{v_W^a v_i}{v_W}\frac{1}{v_i}\tilde{v}^* = \frac{v_W^a}{v_W}v^*, \tag{A22}$$

where we use the fact that $\tilde{v}^* = v^*$ arising from the requirement:

$$\sum_{i=1}^{N} W(\tilde{v}^*)\tilde{v}^* = \sum_{i=1}^{N} W(\tilde{v}_i)\tilde{v}_i = \tilde{v}_W = v_W = \sum_{i=1}^{N} W(v_i)v_i = \sum_{i=1}^{N} W(v^*)v^*. \tag{A23}$$

The properties of weighted volume-preserving size averaging after weighted composition averaging are thus

$$\check{v}_i = \sum_{a=1}^{A} \check{v}_i^a = \sum_{a=1}^{A} \frac{v_W^a}{v_W}v^* = v^* \text{ (particle volumes are average volume)} \tag{A24}$$

$$\check{v}_W^a = \sum_{i=1}^{N} W(\check{v}_i)\check{v}_i^a = \sum_{i=1}^{N} W(v^*)\frac{v_W^a}{v_W}v^* = v_W^a \quad \text{(weighted total species volumes are preserved)} \tag{A25}$$

$$\check{v}_W = \sum_{a=1}^{A} \check{v}_W^a = \sum_{a=1}^{A} v_W^a = v_W \text{ (weighted total volume is preserved)} \tag{A26}$$

$$\check{N}_W = \sum_{i=1}^{N} W(\check{v}_i) = \sum_{i=1}^{N} W(v^*) = \tilde{N}_W \neq N_W \quad \text{(weighted total number is not preserved)} \tag{A27}$$

$$\frac{\check{v}_i^a}{\check{v}_i} = \frac{v_W^a}{v_W}v^*\frac{1}{v^*} = \frac{v_W^a}{v_W} \quad \text{(per-particle species ratios are equal to weighted total species ratios)} \tag{A28}$$

$$\frac{\check{v}_i}{\check{v}_W} = \frac{v^*}{v_W} \text{ (particle volume ratios of weighted total volume are all equal).} \tag{A29}$$

From the above results we see that combined weighted volume-preserving size and composition averaging gains the additional property of preserving weighted total species volumes, but still does not preserve the total number.

Note that we could preserve both volume and number concentrations exactly by also adjusting W to $\check{W} = \alpha W$ so that

$$\sum_{i=1}^{N} \check{W}(v^*) = \sum_{i=1}^{N} W(v_i) \tag{A30}$$

$$\sum_{i=1}^{N} \check{W}(v^*)v^* = \sum_{i=1}^{N} W(v_i)v_i. \tag{A31}$$

This requires

$$v^* = \frac{\sum_{i=1}^{N} W(v_i)v_i}{\sum_{i=1}^{N} W(v_i)} \tag{A32}$$

$$\alpha = \frac{\sum_{i=1}^{N} W(v_i)}{\sum_{i=1}^{N} W(v^*)}. \tag{A33}$$

As averaging is performed per bin, however, this would result in different α (and thus different $\check{W}$) for each bin, making this feasible only if a single bin is being used that contains all particles.

A4. Size Averaging (Number-Preserving Version)

This section presents the alternative size-averaging procedure that preserves total number, in contrast to the volume- or mass-preserving variant in section A2.

We use the notation from section A1. The weighted size-averaged particles (number-preserving version) are specified by their species volumes $\mathring{v}_i^a$, which are defined by:

$$\mathring{v}_i^a = \frac{v_i^a}{v_i} v^\circ, \tag{A34}$$

where v° satisfies:

$$N_W = \sum_{i=1}^{N} W(v_i) = \sum_{i=1}^{M} W(v^\circ). \tag{A35}$$

If W is continuous then at least one v° exists in $\left[\min_{i=1}^{N}(v_i), \max_{i=1}^{N}(v_i)\right]$. If $W(v)$ is also strictly monotonic (as is the case for the weighting schemes used in this paper) then v° is unique.

From the above definition, the properties of weighted size averaging (number-preserving version) are

$$\mathring{v}_i = \sum_{a=1}^{A} \mathring{v}_i^a = \sum_{a=1}^{A} \frac{v_i^a}{v_i} v^\circ = v^\circ \text{ (particle volumes are weighted-average volume)} \tag{A36}$$

$$\mathring{v}_W^a = \sum_{i=1}^{N} W(\mathring{v}_i)\mathring{v}_i^a = \sum_{i=1}^{N} W(v^\circ)\frac{v_i^a}{v_i} v^\circ \neq v_W^a \quad \text{(weighted total species volumes are not preserved)} \tag{A37}$$

$$\mathring{v}_W = \sum_{i=1}^{N}\sum_{a=1}^{A} W(\mathring{v}_i)\mathring{v}_i^a = \sum_{i=1}^{N}\sum_{a=1}^{A} W(v^\circ)\frac{v_i^a}{v_i} v^\circ = \sum_{i=1}^{N} W(v^\circ) v^\circ \neq v_W \quad \text{(weighted total volume is not preserved)} \tag{A38}$$

$$\mathring{N}_W = \sum_{i=1}^{N} W(\mathring{v}_i) = \sum_{i=1}^{N} W(v^\circ) = N_W \text{ (weighted total number is preserved)} \tag{A39}$$

$$\frac{\mathring{v}_i^a}{\mathring{v}_i} = \frac{\frac{v_i^a}{v_i} v^\circ}{v^\circ} = \frac{v_i^a}{v_i} \text{ (per-particle species ratios are preserved)} \tag{A40}$$

$$\frac{\mathring{v}_i}{\mathring{v}_W} = \frac{v^\circ}{\mathring{v}_W} \text{ (particle volume ratios of total volume are all equal).} \tag{A41}$$

From the above derivations we see that size averaging (number-preserving version) does preserve the total number and per-particle compositions, while setting all particles sizes to a single value, but that total volume is not preserved.

A5. Combining Size and Composition Averaging (Number-Preserving Version)

Combining number-preserving size and composition averaging does not result in additional preservation properties, unlike the volume-preserving case (section A3). This can be seen by calculating the particle compositions $\mathring{\tilde{v}}_i^a$ obtained if weighted size averaging is done after weighted composition averaging:

$$\mathring{\tilde{v}}_i^a = \frac{\tilde{v}_i^a}{\tilde{v}_i} \tilde{v}^\circ = \frac{v_W^a v_i}{v_W} \frac{1}{v_i} \tilde{v}^\circ = \frac{v_W^a}{v_W} v^\circ, \tag{A42}$$

where we use the fact that $\tilde{v}^\circ = v^\circ$ arising from the requirement

$$\sum_{i=1}^{N} W(\tilde{v}^\circ) = \sum_{i=1}^{N} W(\tilde{v}_i) = \tilde{N}_W = N_W = \sum_{i=1}^{N} W(v_i) = \sum_{i=1}^{N} W(v^\circ). \tag{A43}$$

The properties of weighted number-preserving size averaging after weighted composition averaging can now be found:

$$\mathring{v}_i = \sum_{a=1}^{A} \mathring{v}_i^a = \sum_{a=1}^{A} \frac{v_W^a}{v_W} v^\circ = v^\circ \text{ (particle volumes are average volume)} \tag{A44}$$

$$\mathring{v}_W^a = \sum_{i=1}^{N} W(\mathring{v}_i)\mathring{v}_i^a = \sum_{i=1}^{N} W(v^\circ)\frac{v_W^a}{v_W} v^\circ \neq v_W^a \quad \text{(weighted total species volumes are not preserved)} \tag{A45}$$

$$\mathring{v}_W = \sum_{a=1}^{A} \mathring{v}_W^a = \sum_{a=1}^{A}\sum_{i=1}^{N} W(v^\circ)\frac{v_W^a}{v_W} v^\circ = \sum_{i=1}^{N} W(v^\circ)v^\circ = \mathring{v}_W \neq v_W \quad \text{(weighted total volume is not preserved)} \tag{A46}$$

$$\mathring{N}_W = \sum_{i=1}^{N} W(\mathring{v}_i) = \sum_{i=1}^{N} W(v^\circ) = \tilde{N}_W = N_W \text{ (weighted total number is preserved)} \tag{A47}$$

$$\frac{\mathring{v}_i^a}{\mathring{v}_i} = \frac{v_W^a}{v_W} v^\circ \frac{1}{v^\circ} = \frac{v_W^a}{v_W} \quad \text{(per-particle species ratios are equal to the weighted total species ratios)} \tag{A48}$$

$$\frac{\mathring{v}_i}{\mathring{v}_W} = \frac{v^\circ}{\mathring{v}_W} \text{ (particle volume ratios of weighted total volume are all equal).} \tag{A49}$$

From the above derivations we see that combining number-preserving size and composition averaging does not gain any preservation properties, in contrast to the combination of volume-preserving size and composition averaging.

As for the volume-preserving version, the number-preserving size-averaging method can use a scaled weighting function to preserve both total volume and number when combined with composition averaging in the single-bin case. See the end of section A3 for a discussion of how this can be done.

Acknowledgments
The authors acknowledge funding from the National Science Foundation under grants NSF ATM 07-39404 and NSF ATM 09-34491. A portion of this research was supported by the U.S. Department of Energy, Office of Science, Biological and Environmental Research as part of the Atmospheric System Research program under grants DE-SC0003921 and DE-SC0011771. The Pacific Northwest National Laboratory is operated for DOE by Battelle Memorial Institute under contract DE-AC05-76RL01830. Model output data can be obtained by contacting N. Riemer (nriemer@illinois.edu).

References

Andreae, M. O., and D. Rosenfeld (2008), Aerosol-cloud-precipitation interactions. Part 1. The nature and sources of cloud-active aerosols, *Earth Sci. Rev.*, *89*(1–2), 13–41, doi:10.1016/j.earscirev.2008.03.001.

Babb, D. M., and J. Verlinde (1999), Vertical velocity statistics in continental stratocumulus as measured by a 94 GHz radar, *Environ. Res. Lett.*, *26*(8), 1177–1180.

Bahadur, R., L. M. Russell, M. Z. Jacobson, K. Prather, A. Nenes, P. Adams, and J. H. Seinfeld (2012), Importance of composition and hygroscopicity of BC particles to the effect of BC mitigation on cloud properties: Application to California conditions, *J. Geophys. Res.*, *117*, D09204, doi:10.1029/2011JD017265.

Bauer, S., D. Wright, D. Koch, E. Lewis, R. McGraw, L. Chang, S. Schwartz, and R. Ruedy (2008), MATRIX (Multiconfiguration Aerosol TRacker of mIXing state): An aerosol microphysical module for global atmospheric models, *Atmos. Chem. Phys.*, *8*, 6003–6035.

Bewley, J. L., and S. Lasher-Trapp (2011), Progress on predicting the breadth of droplet size distributions observed in small cumuli, *J. Atmos. Sci.*, *68*, 2921–2929.

Bond, T. C., et al. (2013), Bounding the role of black carbon in the climate system: A scientific assessment, *J. Geophys. Res. Atmos.*, *118*, 5380–5552, doi:10.1002/jgrd.50171.

Cahill, J. F., K. Suski, J. H. Seinfeld, R. A. Zaveri, and K. A. Prather (2012), The mixing state of carbonaceous aerosol particles in Northern and Southern California measured during CARES and CalNex 2010, *Atmos. Chem. Phys.*, *12*(22), 10,989–11,002, doi:10.5194/acp-12-10989-2012.

Carslaw, K. S., et al. (2013), Large contribution of natural aerosols to uncertainty in indirect forcing, *Nature*, *503*, 67–71, doi:10.1038/nature12674.

Chen, J., Y. Liu, M. Zhang, and Y. Peng (2016), New understanding and quantification of the regime dependence of aerosol-cloud interaction for studying aerosol indirect effects, *Geophys. Res. Lett.*, *43*, 1780–1787, doi:10.1002/2016GL067683.

Chen, W., Y. H. Lee, P. J. Adams, A. Nenes, and J. H. Seinfeld (2010), Will black carbon mitigation dampen aerosol indirect forcing?, *Geophys. Res. Lett.*, *37*, L09801, doi:10.1029/2010GL042886.

Ching, J., N. Riemer, and M. West (2012), Impacts of black carbon mixing state on black carbon nucleation scavenging: Insights from a particle-resolved model, *J. Geophys. Res.*, *117*, D23209, doi:10.1029/2012JD018269.

Conant, W., A. Nenes, and J. Seinfeld (2002), Black carbon radiative heating effects on cloud microphysics and implications for aerosol indirect forcing, 1, Extended Köhler theory, *J. Geophys. Res*, *107*(D21), 4604, doi:10.1029/2002JD002094.

DeVille, R. E. L., N. Riemer, and M. West (2011), Weighted Flow Algorithms (WFA) for stochastic particle coagulation, *J. Comput. Phys.*, *230*(23), 8427–8451, doi:10.1016/j.jcp.2011.07.027.

Dusek, U., G. P. Reischl, and R. Hitzenberger (2006), CCN activation of pure and coated carbon black particles, *Environ. Sci. Technol.*, *40*(4), 1223–1230, doi:10.1021/es0503478.
Feichter, J., and P. Stier (2012), Assessment of black carbon radiative effects in climate models, *Wiley Interdiscip. Rev. Clim. Change*, *3*, 359–370, doi:10.1002/wcc.180.
Feingold, G., W. L. Eberhard, D. E. Veron, and M. Previdi (2003), First measurements of the Twomey indirect effect using ground-based remote sensors, *Geophys. Res. Lett.*, *30*(6), 1287, doi:10.1029/2002GL016633.
Fierce, L., N. Riemer, and T. C. Bond (2015), Explaining variance in black carbon's aging timescale, *Atmos. Chem. Phys.*, *15*, 3173–3191.
Furutani, H., M. Dallosto, G. Roberts, and K. Prather (2008), Assessment of the relative importance of atmospheric aging on CCN activity derived from field observations, *Atmos. Environ.*, *42*(13), 3130–3142.
Hitzenberger, R., A. Berner, H. Giebl, R. Kromp, S. M. Larson, A. Rouc, A. Koch, S. Marischka, and H. Puxbaum (1999), Contribution of carbonaceous material to cloud condensation nuclei concentrations in European background (Mt. Sonnblick) and urban (Vienna) aerosols, *Atmos. Environ.*, *33*, 2647–2659.
Howell, W. E. (1949), The growth of cloud drops in uniformly cooled air, *J. Meteorol.*, *6*, 134–149.
Jacobson, M. Z. (2001), Strong radiative heating due to the mixing state of black carbon in atmospheric aerosols, *Nature*, *409*, 695–697.
Jacobson, M. Z. (2010), Short-term effects of controlling fossil-fuel soot, biofuel soot and gases, and methane on climate, arctic ice, and air pollution health, *J. Geophys. Res.*, *115*, D14209, doi:10.1029/2009JD013795.
Kaiser, J., J. Hendricks, M. Righi, N. Riemer, R. A. Zaveri, S. Metzger, and V. Aquila (2014), The MESSy aerosol submodel MADE3 (v2. 0b): Description and a box model test, *Geosci. Model Dev.*, *7*, 1137–1157.
Liu, X., et al. (2012), Toward a minimal representation of aerosols in climate models: Description and evaluation in the Community Atmosphere Model CAM5, *Geosci. Model Dev.*, *5*, 709–739.
Liu, Y., and P. H. Daum (2000), Spectral dispersion of cloud droplet size distributions and the parameterization of cloud droplet effective radius, *Geophys. Res. Lett.*, *27*, 1903–1906.
Liu, Y., and P. H. Daum (2002), Indirect warming effect from dispersion forcing, *Nature*, *419*, 580–581.
Liu, Y., and P. H. Daum (2004), Parameterization of the autoconversion process. Part I: Analytical formulation of the Kessler-type parameterizations, *J. Atmos. Sci.*, *61*, 1539–1548.
Lu, C., Y. Liu, S. Niu, and A. M. Vogelmann (2012), Observed impacts of vertical velocity on cloud microphysics and implications for aerosol indirect effects, *Geophys. Res. Lett*, *39*, L21801, doi:10.1029/2012GL053599.
Ma, X., F. Yu, and G. Luo (2012), Aerosol direct radiative forcing based on GEOS-Chem-APM and uncertainties, *Atmos. Chem. Phys.*, *12*, 5563–5581.
Majeed, M. A., and A. S. Wexler (2001), Microphysics of aqueous droplets in clouds and fogs as applied to PM-fine modeling, *Atmos. Environ.*, *35*, 1639–1653.
Martin, G. M., D. W. Johnson, and A. Spice (1994), The measurement and parameterization of effective radius of droplets in warm marine stratocumulus, *J. Atmos. Sci.*, *51*, 1823–1842.
Matsui, H., M. Koike, Y. Kondo, N. Moteki, J. D. Fast, and R. A. Zaveri (2013), Development and validation of a black carbon mixing state resolved three-dimensional model: Aging processes and radiative impact, *J. Geophys. Res. Atmos.*, *118*, 2304–2326, doi:10.1029/2012JD018446.
McFarquhar, G. M., and A. J. Heymsfield (2001), Parameterization of INDOEX microphysical measurements and calculations of cloud susceptibility: Applications for climate studies, *J. Geophys. Res.*, *106*, 28,675–28,698.
McMeeking, G. R., W. T. Morgan, M. Flynn, E. J. Highwood, K. Turnbull, J. Haywood, and H. Coe (2011), Black carbon aerosol mixing state, organic aerosols and aerosol optical properties over the United Kingdom, *Atmos. Chem. Phys.*, *11*(17), 9037–9052, doi:10.5194/acp-11-9037-2011.
Moffet, R., and K. Prather (2009), In-situ measurements of the mixing state and optical properties of soot with implications for radiative forcing estimates, *Proc. Natl. Acad. Sci. U.S.A.*, *106*(29), 11,872–11,877.
Mordy, W. (1959), Computations of the growth by condensation of a population of cloud droplets, *Tellus*, *11*, 16–44.
Moteki, N., Y. Kondo, Y. Miyazaki, N. Takegawa, Y. Komazaki, G. Kurata, T. Shirai, D. R. Blake, T. Miyakawa, and M. Koike (2007), Evolution of mixing state of black carbon particles: Aircraft measurements over the Western Pacific in March 2004, *Geophys. Res. Lett*, *34*, L11803, doi:10.1029/2006GL028943.
Nenes, A., S. Ghan, H. Abdul-Razzak, P. Chuang, and J. H. Seinfeld (2001), Kinetic limitations on cloud droplet formation and impact on cloud albedo, *Tellus B*, *53*, 133–149.
Ohring, G., R. Wielicki, R. Spencer, B. Emery, and R. Dalta (2005), Satellite instrument calibration for measuring global climate change: Report of a workshop, *Bull. Am. Meteorol. Soc.*, *86*, 1303–1313, doi:10.1175/BAMS-86-9-1303.
Peng, Y., U. Lohmann, and R. Leaitch (2005), Importance of vertical velocity variations in the cloud droplet nucleation process of marine stratus clouds, *J. Geophys. Res.*, *110*, D21213, doi:10.1029/2004JD004922.
Pruppacher, H. R., and J. D. Klett (1997), *Microphysics of Clouds and Precipitation*, Kluwer Acad., Dordrecht, Netherlands.
Ramanathan, V., and G. Carmichael (2008), Global and regional climate changes due to black carbon, *Nat. Geosci.*, *1*, 221–227.
Reutter, P., H. Su, J. Trentmann, M. Simmel, D. Rose, S. Gunthe, H. Wernli, M. Andreae, and U. Pöschl (2009), Aerosol- and updraft-limited regimes of cloud droplet formation: Influence of particle number, size and hygroscopicity on the activation of cloud condensation nuclei (CCN), *Atmos. Chem. Phys.*, *9*, 7067–7080.
Riemer, N., M. West, R. Zaveri, and R. Easter (2009), Simulating the evolution of soot mixing state with a particle-resolved aerosol model, *J. Geophys. Res.*, *114*, D09202, doi:10.1029/2008JD011073.
Riemer, N., M. West, R. Zaveri, and R. Easter (2010), Estimating black carbon aging time-scales with a particle-resolved aerosol model, *J. Aerosol Sci.*, *41*, 143.
Rotstayn, L. D., and Y. Liu (2003), Sensitivity of the first indirect aerosol effect to an increase of cloud droplet spectral dispersion with droplet number concentration, *J. Clim.*, *16*, 3476–3481.
Schell, B., I. J. Ackermann, F. S. Binkowski, and A. Ebel (2001), Modeling the formation of secondary organic aerosol within a comprehensive air quality model system, *J. Geophys. Res.*, *106*, 28,275–28,293.
Seinfeld, J. (2008), Black carbon and brown clouds, *Nat. Geosci.*, *1*, 15–16, doi:10.1038/ngeo.2007.62.
Seinfeld, J. H., and S. Pandis (1997), *Atmospheric Chemistry and Physics: From Air Pollution to Climate Change*, John Wiley, New York.
Slingo, A. (1990), Sensitivity of the Earth's radiation budget to changes in low clouds, *Nature*, *343*, 49–51.
Stevens, B., and G. Feingold (2009), Untangling aerosol effects on clouds and precipitation in a buffered system, *Nature*, *461*(7264), 607–613.
Twomey, S. (1991), Aerosols, clouds and radiation, *Atmos. Environ.*, *254*, 2435–2442.

United States Environmental Protection Agency (2012), Report to congress on black carbon, *Tech. Rep.*, United States Environ. Prot. Agency, Research Triangle Park, N. C. [Available at https://www3.epa.gov/blackcarbon/2012report/fullreport.pdf.]

Wang, Z. L., H. Zhang, and X. Y. Zhang (2014), Black carbon reduction will weaken the aerosol net cooling effect, *Atmos. Chem. Phys. Discuss.*, *14*, 33,117–33,141.

Zaveri, R., J. Barnard, R. Easter, N. Riemer, and M. West (2010), Particle-resolved simulation of aerosol size, composition, mixing state, and the associated optical and cloud condensation nuclei activation properties in an evolving urban plume, *J. Geophys. Res*, *115*, D17210, doi:10.1029/2009JD013616.

Zaveri, R. A., and L. K. Peters (1999), A new lumped structure photochemical mechanism for large-scale applications, *J. Geophys. Res.*, *104*, 30,387–30,415.

Zaveri, R. A., R. C. Easter, and L. K. Peters (2005a), A computationally efficient Multicomponent Equilibrium Solver for Aerosols (MESA), *J. Geophys. Res.*, *110*, D24203, doi:10.1029/2004JD005618.

Zaveri, R. A., R. C. Easter, and A. S. Wexler (2005b), A new method for multicomponent activity coefficients of electrolytes in aqueous atmospheric aerosols, *J. Geophys. Res.*, *110*, D02210, doi:10.1029/2004JD004681.

Zaveri, R. A., R. C. Easter, J. D. Fast, and L. K. Peters (2008), Model for Simulating Aerosol Interactions and Chemistry (MOSAIC), *J. Geophys. Res.*, *113*, D13204, doi:10.1029/2007JD008782.

Zhang, H., S. P. DeNero, D. K. Joe, H. H. Lee, S. H. Chen, J. Michalakes, and M. J. Kleeman (2014), Development of a source oriented version of the WRF/Chem model and its application to the California regional $PM_{10}/PM_{2.5}$ air quality study, *Atmos. Chem. Phys.*, *14*, 485–503.